Delft University of Technology
Geoscience and Remote Sensing

Master Thesis Applied Physics

The effect of land-surface heterogeneity on mixing in the Stable Boundary Layer

Supervisors
Prof.dr.ir. B.J.H. van de Wiel
Dr.ir. J.A. van Hooft

Author
Myrthe Breedijk

Graduation Committee
Prof.dr.ir. B.J.H. van de Wiel
Dr. S.R. de Roode
Dr.ir. D.J. Verschuur
Dr.ir. J.A. van Hooft

to obtain the degree of Master of Science
at the Delft University of Technology,
to be defended publicly on June 18, 2021 at 15:00 PM.

June 2021

This thesis is in partial fulfillment of the requirements for the degree of Master of Science in Applied Physics at the faculty of Applied Sciences at Delft University of Technology. The research has been conducted in the department of Geoscience & Remote Sensing at the faculty of Civil Engineering. This project is carried out under the supervision of Dr.ir. J.A. van Hooft and Prof.dr.ir. B.J.H. van der Wiel.

Abstract

This study aims to look into the effect of small-scale surface heterogeneity on the mixing properties within the stable boundary layer (SBL) and the impact of different configurations of the heterogeneity on this mixing. The motivation for this research is to better understand the turbulent mixing phenomena in the SBL and to be able to represent the mixing more accurate in weather prediction models. In the current models, this mixing is highly uncertain or even missing. It is likely that this mixing is driven by thermal memories that are spatially distributed over the land-surface in the form of surface heterogeneity. These surface heterogeneities (e.g. ditches or roads) effectively store heat during the day and then turn into heat sources, driving turbulent mixing, during the night. A simulation with surface heat sources in an idealized SBL is setup and four case studies are performed. The simulations show that the heat sources clearly influence the mixing in the SBL. A buoyancy plume is formed above a heat source. The plumes of two heat sources are attracted towards each other. At smaller distances the plumes even merge and form a single plume. In the three-dimensional simulations, the distance between the heat sources has an influence on their effect on the SBL. At small distances, the kinetic energy in the system decreases with increasing distances between two heat sources. At larger distances this decrease appears to level off. Apparently, the bending and merging of the plumes allows turbulent length scales to increase, causing the effect of the buoyancy sources to be larger. To verify these simulation results, a field experiment is conducted. An infrared camera pointing at a vertical high-emissivity cloth was able to capture the two-dimensional (vertical and horizontal) air temperature pattern above heat sources. The merging effect between two plumes is also observed in this field experiment. At small distances a single merged heat plume was visible above two heat sources and at larger distances two separated heat plumes are formed.

Contents

Chapter 1

Introduction

During daytime the sun heats the Earth's surface and consequently the air adjacent to it. The warm air will rise, this causes a deep (ca. $1-2\,\mathrm{km}$) turbulent mixing layer called the convective boundary layer (CBL). During nighttime loss of thermal radiation at the Earth's surface causes the surface and consequently the adjacent air to cool, giving rise to a stable stratification. Depending on the magnitude of the ambient wind speed, which causes vertical mixing of air, the strength of this stratification varies. In this report we only consider nights without ambient wind forcing. Then the two potential mechanisms for driving turbulence (wind shear and positive buoyancy forces [1]) are absent and thus turbulent mixing seems to be absent. The lower part of the atmosphere is then called a (very) stable boundary layer (SBL). Surprisingly, even in absence of any wind the air slowly keeps moving on multiple scales within the SBL. Therefore heat, momentum and moisture are still transported through the boundary layer. This so-called 'unseen mixing' is highly uncertain or even missing in current large-scale weather forecasting under very stable conditions [2, 3]. This is also due to the fact that no general theory exists about why the atmosphere is able to sustain turbulence under conditions of cold nights with weak or no winds. This uncertainty causes differences of 5 to 10 Kelvin between various plausible mixing schemes in weather predictions and makes it hard to create accurate weather forecasts [4–6]. Therefore, it would be highly desirable to better understand the turbulent mixing phenomena in stable boundary layers, which is the purpose of this present study.

It is likely that this mixing originates from thermal memories that are spatially distributed over the land-surface in the form of surface heterogeneity [7, 8]. A surface heterogeneity, like a ditch or a road, can effectively store heat during the day. This stored heat can cause positive buoyancy forces that drive turbulent mixing during nighttime. An example of differences in surface temperature of ditches through a meadow is shown in figure 1.1.

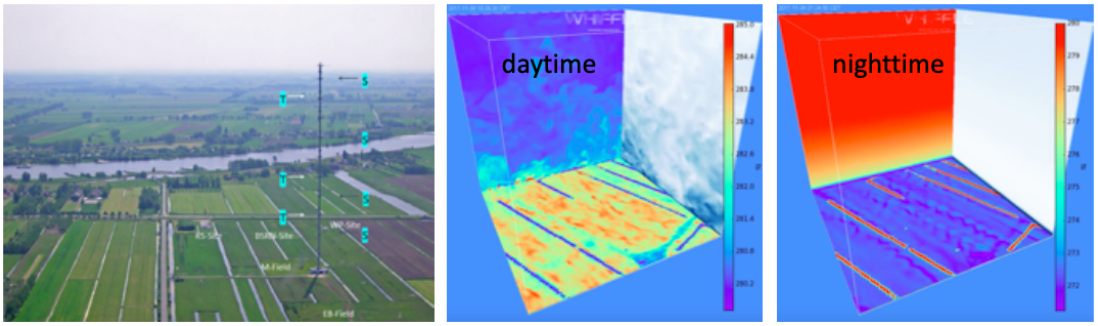

FIGURE 1.1: A visualisation of the impact of the diurnal cycle on the surface temperature of ditches through a meadow. On the left the real-life site at Cabauw (Utrecht, The Netherlands, 51°58'11.2"N, 4°55'34.6) is shown. The middle and right figures are results of Large Eddy Simulations (GPU-mode, fixed grid) during daytime and nighttime respectively. It can be seen that the ditches are warmer than the meadow during the night. Figure adapted from personal communication with Van de Wiel, (2021).

The temperature measurements during a full diurnal cycle at five nearby locations (see figure 1.2) also point out the likeliness of surface heterogeneity influencing the local temperature during nighttime. During daytime the temperatures do not show large difference between the different locations, because of the large-scale mixing. However, during nighttime large differences between the different locations are observed. As large-scale forcings were uniform during that night (e.g. no clouds), it is likely that this is due to the variation in surface properties between the locations.

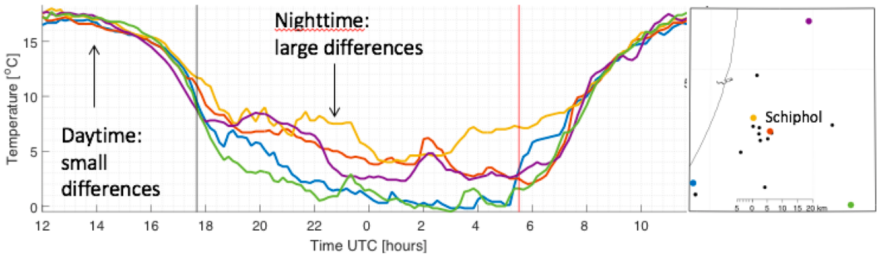

FIGURE 1.2: Temperature recordings of five sites near Schiphol (Noord-Holland, The Netherlands, 52°19'10.5"N, 4°45'38.6). Clear temperature fluctuations are visible during nighttime. Figure adapted from personal communication with Van de Wiel (2021).

Surface heterogeneities are typically smaller in scale than the used grid size (10-100 km [9]) in Numerical Weather Prediction (NWP) models, which requires their effects to be parametrized in the models. The final goal within this field of research is to correctly represent surface heterogeneity by a parametrization in NWP models. This research will set the first steps towards this final goal by answering the following research questions:

What is the effect of small-scale surface heterogeneity on the mixing properties within the stable boundary layer? What impact do different configurations of the heterogeneity have on this mixing?

To answer those questions, insights from various numerical simulations and from an observational field study will be combined.

In Chapter 2 an overview of the relevant theory will be given and in Chapter 3 the simulation and experimental methods will be described. Chapter 4 gives the results accompanied with the discussion. Finally, Chapter 5 will conclude this report and give recommendations for further research.

Chapter 2

Theory

2.1 The atmospheric boundary layer (ABL)

The atmospheric boundary layer (ABL) is defined as the lowest part of the troposphere that is directly influenced by the presence of the Earth's surface, and responds to surface forcing within a timescale of about an hour or less [10]. The depth of the layer can range from a few meters to several kilometers depending on the local meteorology. Usually, a lot of turbulence is present in this boundary layer. Turbulence can be generated by wind shear or by buoyancy forces. In presence of wind, turbulence is created when a flow passes surface roughness (e.g. trees, houses and grass), the wind shear then creates turbulence. In presence of temperature fluctuations (e.g. heating by the sun), turbulence is caused by buoyancy forces. Warm and lighter air parcels in a colder and denser environment will be drifted upward (and vice versa) by the gravity field creating turbulence. Turbulence is characterized by swirls, also called eddies (see figure 2.1). Turbulence consists of many eddies with different sizes that interact with each other.

During a typical day (e.g. no storm or heavy rain) the sun heats the surface and buoyancy is the main mechanism driving turbulence. Typical for this daytime ABL is that large-scale mixing takes place caused by large eddies. The depth of the turbulent mixing layer is typically $1 - 2\,\text{km}$. Mostly, during nighttime surface cooling leads to suppression of turbulence by a negative buoyancy force ('the stratification of the air'), then only forced convection can drive turbulence. This causes much smaller eddies and the depth of the turbulent mixing layer is typically $100 - 200\,\text{m}$. However, during nights with very weak or no wind the forced convection is also suppressed by the effect of the negative buoyancy and turbulence seems to vanish (strongly stably stratified boundary layer). In reality the air slowly keeps moving around and turbulent mixing still takes place. The hypothesis of this research is that turbulent mixing during stable nights is caused by surface heterogeneity acting as spatially distributed subsurface thermal memories. The

research presented in this report focuses on the processes in the stable boundary layer, therefore the following theory will focus mainly on the stable boundary layer.

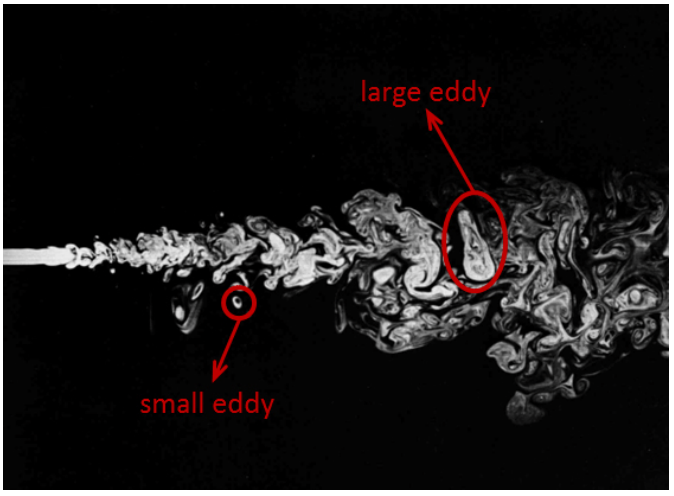

FIGURE 2.1: An example of turbulent structures with the visualization of different sized eddies. Figure adapted from [11].

An important characteristic of the ABL is its so-called static stability. In a horizontal uniform atmosphere, the static stability relates to the vertical density profile (and hence the temperature profile). If the density decreases (and the temperature increases) with height, the atmosphere is said to be stable: a parcel will not spontaneously move in the gravity field. Likewise, if the density of the air increases (and the temperature decreases) with height, the atmosphere is said to be unstable: a parcel will spontaneously move in the gravity field.

Thus, the static stability of the boundary is assessed by looking at the acceleration caused by the buoyancy of an air parcel when vertically displaced. The buoyancy force $b\,[\mathrm{ms}^{-2}]$ on an adiabatic parcel (no heat/mass transfer) is often expressed in terms of the potential temperature $\theta\,[\mathrm{K}]$ [12]:

$$b = \frac{g}{\theta_e}(\theta_p - \theta_e) \tag{2.1}$$

where $g\,[\mathrm{ms}^{-2}]$ is the gravitational constant and $\theta_p\,[\mathrm{K}]$ and $\theta_e\,[\mathrm{K}]$ the potential temperature of respectively the parcel and the environment. The potential temperature is a conserved quantity for adiabatic processes and is therefore widely used in atmospheric physics. The potential temperature of an adiabatic parcel with absolute temperature $T_p\,[\mathrm{K}]$ at pressure $p\,[\mathrm{Pa}]$ in a dry atmosphere (moisture neglected) is defined as [13]:

$$\theta = T_p \left(\frac{p_0}{p}\right)^{R_d/c_p} \tag{2.2}$$

where $p_0 = 1000\,\mathrm{hPa}$ is a standard reference pressure, $R_d\,[\mathrm{Jkg}^{-1}\mathrm{K}^{-1}]$ is the gas constant of dry air and $c_p\,[\mathrm{Jkg}^{-1}\mathrm{K}^{-1}]$ the specific heat capacity of dry air.

During cold nights the surface and consequently the air above is cooled, causing the atmosphere to stabilize. This causes an increase of potential temperature with height. This can be expressed by the condition of the Brunt-Väisälä frequency $N\,[\mathrm{s}^{-1}]$ of a stable atmosphere [13]:

$$N^2 = \frac{g}{\theta_e}\frac{d\theta_e}{dz} > 0\,\mathrm{s}^{-2} \tag{2.3}$$

where $\theta_e\,[\mathrm{K}]$ is the potential temperature of the environment and $d\theta_e/dz\,[\mathrm{Km}^{-1}]$ the change in this potential temperature over a vertical distance $dz\,[\mathrm{m}]$.

Looking at equation 2.1 and the condition in equation 2.3, it can be concluded that when a parcel moves away from its original position in a stably stratified atmosphere, the buoyancy force will exert a force in the *opposite* direction of displacement. From this it is then concluded that the background stratification is stable to perturbations.

2.2 Surface energy budget (SEB)

During daytime the Earth's surface is heated. For different types of surfaces (e.g. grass, soil, roads and ditches) this heating and the partitioning hereof will have different effects. The heat can be stored at the upper part of the surface (grass isolates the soil), it can be transported to and stored deeper in the surface (thermal conduction in bare soil), it can warm the air or it can cause evaporation. All these phenomena are examples of different components of the surface energy budget. Because the partitioning of energy fluxes over the components will be different for different surfaces, the surface temperature will also be different.

During nighttime the surface will be cooled. However, some surfaces will remain warmer due to significant heat storage during the day (e.g. ditches and asphalt). Because they are warmer, they can act like sources for buoyancy forces. The air adjacent to the warm surface will be heated and the warm air starts rising, which sets in a circulation and (weak) turbulent motions. Surface heterogeneities can thus cause local turbulence driven by the mechanisms of buoyancy.

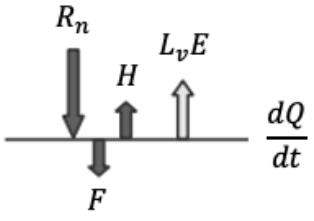

FIGURE 2.2: A schematical overview of the surface energy balance. The dark and light gray arrows indicate the transport through energy and water respectively. Figure adapted from [1].

The surface energy budget will now be explained and the role of surface heterogeneity in all terms will be discussed [1]:

$$\frac{dQ}{dt} = R_n - F - H - L_v E \tag{2.4}$$

- $Q\,[\mathrm{Jm}^{-2}]$ is the total heat, expressed in energy per square meter, stored in the surface layer (e.g. a vegetation layer).
- $R_n\,[\mathrm{Wm}^{-2}]$ is the net surface radiation and is equal to the gain of energy from radiation by the surface.
- $F\,[\mathrm{Wm}^{-2}]$ is the ground heat flux and is equal to the loss of energy by heat conduction through the lower boundary.
- $H\,[\mathrm{Wm}^{-2}]$ is the sensible heat flux and is equal to the loss of energy by heat transfer to the atmosphere.
- $L_v E\,[\mathrm{Wm}^{-2}]$ is the latent heat flux and is equal to the loss of energy due to evaporation into the atmosphere.

In the example above the daytime case is considered. At night signs are typically reversed, e.g. negative $R_n\,[\mathrm{Wm}^{-2}]$.
The sum of the net surface radiation and the ground heat flux is defined as the 'available energy'. The sensible and latent heat flux are both turbulent fluxes, their sum will be referred to as the 'turbulent fluxes'. The available energy and the turbulent flux are now discussed in more detail and the effect of surface heterogeneity on these terms is pointed out.

2.2.1 Available energy

The available energy is a sum of the net radiation and the ground heat flux: $R_n - F$, the minus sign comes from the definition of the direction of the energy that corresponds to a positive value. The role of surface heterogeneity in both terms will be discussed separately.

2.2.1.1 Net radiation

The net radiation R_n is given by the difference between the incoming short- and long-wave radiation and the outgoing short-wave (SW) and long-wave (LW) radiation (all terms in $[\mathrm{Wm}^{-2}]$):

$$R_n = SW_{in} + LW_{in} - SW_{out} - LW_{out} = (1-\alpha)SW_{in} + LW_{in} - LW_{out} \tag{2.5}$$

The effect of heterogeneity in the surface (neglecting the presence of moisture in the atmosphere) on the local net radiation is:

- The incoming short-wave radiation SW_{in} [Wm^{-2}] is the same for all surface, since it only dependents on the short-wave radiation emitted by the sun and the absorption of the radiation by the atmosphere.
- The Earth itself does not radiate short-wave radiation, that is why the outgoing short-wave radiation is given by the incoming short-wave radiation reflected by the surface with an albedo of α [$-$]: $SW_{out} = \alpha SW_{in}$. The surface albedo α [$-$] is strongly variable for different surfaces (see table 2.1), so the outgoing short-wave radiation varies along different surfaces.
- The incoming long-wave radiation LW_{in} [Wm^{-2}] is the same for all surfaces, since it only depends on the radiation emitted by the atmosphere.
- The outgoing long-wave radiation is a sum of the outgoing long-wave radiation produced by the Earth's surface LW_{Earth} [Wm^{-2}] and the reflection of the incoming long-wave radiation LW_{in} [Wm^{-2}]: $LW_{out} = LW_{Earth} + (1 - \epsilon_s)LW_{in}$, where ϵ_s [$-$] is the long-wave emissivity of the surface. Both outgoing long-wave radiation terms differ with varying surface properties. The Earth's long-wave radiation is given by: $LW_{Earth} = \epsilon\sigma T_s$ ($\sigma = 5.67 \cdot 10^{-8}$ [$\mathrm{Wm}^{-2}\mathrm{K}^{-4}$]). Different surfaces have different surface temperatures (as mentioned before) and a different long-wave emissivity (see table 2.1). However, the variability of emissivity is small and the reflected incoming long-wave radiation is almost negligible ($\epsilon_s \approx 1$).

Surface type	Remark	α [$-$]	ϵ_s [$-$]
Ocean	High sun	0.05	0.95
Ocean	Low sun	$0.1 - 0.5$	0.95
Forest	Tropical rain forest	$0.07 - 0.15$	0.98
Grasses		$0.15 - 0.30$	0.96
Soils	Wet clay	$0.10 - 0.2$	0.97
	Dry sandy	$0.2 - 0.4$	0.95
Snow	Fresh	$0.65 - 0.95$	0.95
Urban areas		$0.10 - 0.27$	$0.85 - 0.96$

TABLE 2.1: Typical values for the short-wave albedo α and the long-wave emissivity ϵ_s for different surface types. Table adapted from [1].

2.2.1.2 Ground heat flux

The main mechanism of heat transport into the ground is conduction. The transport of water can also cause heat transport, but the presence of moisture is neglected in this

research. In a homogeneous soil the ground heat flux $F\,[\mathrm{Wm}^{-2}]$ by conduction will be given by Fourier's law [1]:

$$F = -\lambda \frac{\partial T}{\partial z} \tag{2.6}$$

where $\lambda\,[\mathrm{WK}^{-1}\mathrm{m}^{-1}]$ is the thermal conductivity and $\frac{\partial T}{\partial z}\,[\mathrm{Km}^{-1}]$ is vertical temperature gradient inside the soil. This thermal conductivity varies strongly for soils with different properties and other materials, as can be seen in table 2.2.

Soil type	Remark	$\lambda\,[\mathrm{Wm}^{-1}\mathrm{K}^{-1}]$
Sandy soil	Loosely packed (pore fraction 0.4)	0.24
	Tightly packed (pore fraction 0.33)	0.29
Clay soil	Pore fraction 0.4	0.15
Peat soil	Pore fraction 0.9	0.04
Rock		2.9
Ice		2.5
Fresh snow		0.1
Old snow		1.7

TABLE 2.2: Typical values for the conductivity λ of different types of soil. The values correspond to the soil without moisture and are representative for temperatures around $10 - 20\,^{\circ}\mathrm{C}$. Table adapted from [1].

If the surface is water (e.g. a pond or ditch), the system becomes more complex. Now, heat conduction is not the only mode of transport. In the water also flow may occur and the turbulent transport cannot be excluded, making the assessment of the heat flux more complex. An overview of the basic processes in a pond are shown in figure 2.3. Because of simplicity reasons, a constant water temperature is assumed in this study.

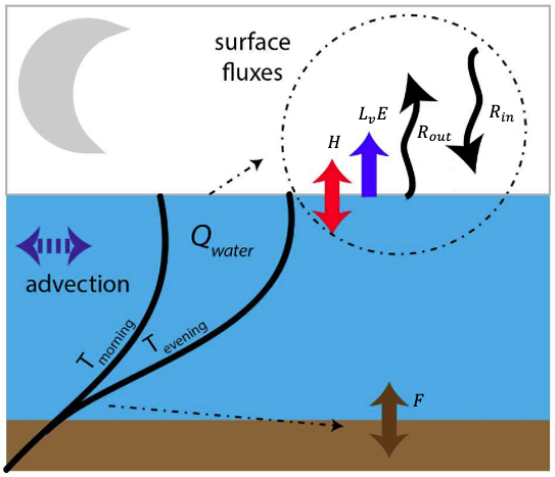

FIGURE 2.3: A schematic overview of the surface energy fluxes at a pond. The black lines show indications of the temperature pattern in the pond in the evening ($T_{evening}$ [K]) and in the morning ($T_{morning}$ [K]). The difference is the released heat Q_{water} [Jm^{-2}]. This is released by a combination of the surface fluxes (H and L_vE) and the net radiation ($R_{in} - R_{out}$) and the ground heat flux (F). Because of the high heat capacity of water, the amplitude of the temperature variation in the water is relatively small. Figure adapted from [14].

2.2.2 Turbulent fluxes

The turbulent fluxes are a sum of the sensible heat flux and the latent heat flux: $H + L_vE$. The sensible heat flux is a consequence of transport of heat to the air and the latent heat flux is a consequence of transport of water vapour. For simplicity reasons, this research will neglect the presence of moisture in the surface and atmosphere, therefore the latent heat flux will not be discussed.

As discussed before, atmospheric turbulence is mostly produced by wind shear and buoyancy. In this study a zero ambient wind is assumed, i.e. focus will lay on heat transport by convection caused by a temperature gradient. The sensible heat flux and the vertical temperature gradient can be linked by defining a turbulent diffusivity [15]:

$$H = \bar{\rho} c_p \overline{w'\theta'} = -\bar{\rho} c_p K_h \frac{\partial \overline{T}}{\partial z} \tag{2.7}$$

where $\bar{\rho}$ [kgm^{-3}] is the average density of air, c_p [Jkg^{-1}K^{-1}] is the heat capacity of air, w' [ms^{-1}] and θ' [K] are the fluctuations in upward velocity and potential temperature and the overbar is used for the average of their product. K_h [m^{2}s^{-1}] is the turbulent diffusivity, this parameter strongly varies for the diurnal cycle and for different heights. The temperature gradient $\frac{\partial \overline{T}}{\partial z}$ [Km^{-1}] will be influenced by the local surface temperature and therefore varies above surface heterogeneity. Note: formally we could also describe horizontal heat transport in a similar way, which is omitted here for brevity.

In this research characteristic scales of turbulent flows will be defined to give a better physical understanding of the system. And proportionality between different physical parameters will be used to simplify the analysis of the system [16]. An example of the definition of characteristic scales for an arbitrary turbulent jet is shown in figure 2.4: $\mathcal{L}\,[\mathrm{m}]$ is the typical length scale and $\mathcal{U}\,[\mathrm{ms}^{-1}]$ the typical velocity scale of the jet. With these characteristic scales and the viscosity of the air $\nu\,[\mathrm{m}^2\mathrm{s}^{-1}]$ a dimensionless group [16] can be defined:

$$Re = \frac{\mathcal{L}\mathcal{U}}{\nu} \tag{2.8}$$

The Reynolds number $Re\,[-]$ is the ratio between the non-linear advection and the molecular friction. For $Re \ll 1\,[-]$ friction is dominant and the flow tends to be laminar, for $Re \gg 1\,[-]$ advection is dominant and the situation is turbulent. The dynamical behavior of the system can now be studied as a function of only the Reynolds number, instead of the three individual parameters $\mathcal{L}\,[\mathrm{m}]$, $\mathcal{U}\,[\mathrm{ms}^{-1}]$ and $\nu\,[\mathrm{m}^2\mathrm{s}^{-1}]$.

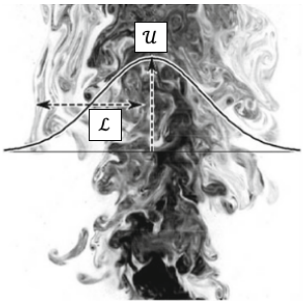

FIGURE 2.4: Definition of the typical length $\mathcal{L}$ and velocity scale $\mathcal{U}$ of a turbulent flow. The Gaussian curve shows the typical velocity profile of a plume in the horizontal direction. Figure adapted from [17].

2.3 Modeling the stable boundary layer

In this section the problems in modeling the SBL nowadays are pointed out. These problems are the motivation to focus on the mixing in the SBL in this research.
In previous research [5] it is demonstrated that today's global Numerical Weather Prediction (NWP) models are not accurate in representing the key features of stable boundary layers. Because of limitations in the computational power, weather models have to rely on coarse grid resolution. Sub-grid processes are ignored or a parametrization is implemented. For example the sub-grid horizontal variation of atmospheric variables (e.g. momentum and temperature) is ignored and the variables are taken constant in the horizontal direction of the grid or a 'tiling approach' is used [18]. This ignorance or poor parametrization is a consequence of a lack of understanding of the physical processes and their coupling in the SBL. A couple of the main problems are [6, 19]:

- The depth of the stable boundary layers are overestimated.

- Near surface temperatures are overestimated.
- The wind turning with height is underestimated.
- The strength of the low-level jet is underestimated and the height above the surface overestimated.
- The wind speed gradient is underestimated.

The main cause of these problems is that NWP models use turbulence simulations which maintain more turbulent diffusion in stable conditions than observed in experiments or in small-scale simulations. Presumably, this over-mixing in stable conditions needs to account for additional contributions to vertical mixing driven by surface heterogeneity, gravity-waves and meso-scale variability [6]. Looking into the effect of surface heterogeneity on the mixing in the SBL is therefore an important part of improving the NWP in stable conditions, as conducted in this research.

Chapter 3

Method

The main goal of this report is to look at the effect of small-scale surface heterogeneity on the mixing properties within the stable boundary layer and the impact of different configurations of the heterogeneity on this mixing. In the following parts of this report the term 'surface heterogeneity' will be used for separated parts of the surface with a higher potential temperature and thus parts that act as a buoyancy source.
The strategy behind the different experiments to answer the research questions is:

1. Design a simulation model that can be used to study surface heterogeneity in an idealized setting of a SBL (see section 3.1.1 *"Numerical solver"* and 3.1.2 *"Modelled physics"*).

2. Validate the model for a simple surface heterogeneity configuration by showing that results are physically 'logical' (see section 3.1.3.1 *"One heat source (2D simulation)"*).

3. Look at the effect of surface heterogeneity on the mixing in the SBL and the effect of their spatial distribution with a case study of a simplified model of the land-surface and the SBL (see section 3.1.3.2 *"Multiple heat sources (2D simulation)"* and 3.1.3.3 *"Multiple heat sources (3D simulation)"*).

4. Propose a conceptual model for a coupling between the land-surface and atmosphere (see section 3.1.3.4 *'The effect of surface-atmosphere coupling (2D simulation)"*).

5. Conduct a field experiment to verify the results of the simulations described in step 3 and 4 (see section 3.2 *"Field experiment method"*).

3.1 Simulation methods

In order to study the effect of surface heterogeneity on mixing in a stable boundary layer a simulation model is made and different case studies are performed. In this section the numerical solver and the modelled physics are explained and finally the case studies are described.

3.1.1 Numerical solver

The numerical solver used for this simulation is called Basilisk [20]. Basilisk is a partial differential equation solver on adaptive Cartesian meshes. The code uses a finite-volume second-order accurate solver for the Navier-Stokes equations under the Boussinesq approximation. The detailed description of the numerical formulations can be found in literature [21–23].

The grid structure used is called a quadtree-based grid for two-dimensional (2D) (x, z) simulations and an octree-based grid for 3D (x, y, z) simulations. In figure 3.1 the spatial structure of the grid cells with varying levels of refinements are shown for 2D. The resolution difference between the levels of refinement are a factor two and Basilisk allows the neighbouring cells to differ one level from each other. The solver uses ghost points that can be defined by the interpolation of the original field values either by up-sampling (blue dots figure 3.1) or down-sampling (red dots figure 3.1). During the simulation, the solver constantly analyses which grid cells need refinement and which cells need coarsening [24]. In the 2D model there are five parameters that determine the refinement process and in the 3D model six: the tolerance for the buoyancy $b\,[\mathrm{ms}^{-2}]$ and the velocity $u_x, u_y, u_z\,[\mathrm{ms}^{-1}]$ (u_y not in the 2D model) and the minimum and maximum level of refinement. These parameters are prescribed to the model by the user.

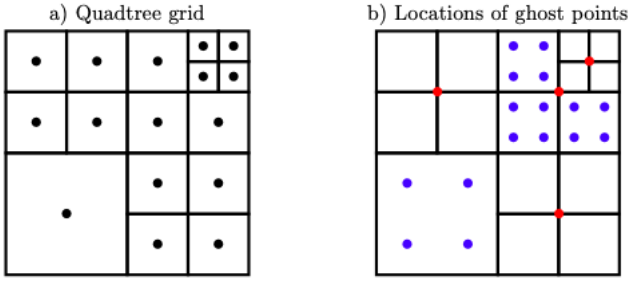

FIGURE 3.1: In figure a and b the 2D spatial structure of the grid cells with varying levels of refinement are shown. The locations of up-sampling (blue dots) and down-sampling (red dots) are shown in figure b. Figure adapted from [25].

3.1.2 Modelled physics

The numerical solver is used for solutions to the equations (conservation laws for mass, heat and momentum) that describe the physical processes in the atmosphere. The solver applies all the relevant laws for every grid cell, these laws are described in this section together with the implemented initial and boundary conditions.

The model needs to solve the incompressible Navier–Stokes equations to determine the pressure $p\,[\mathrm{Pa}]$ and the velocity field $\mathbf{u}\,[\mathrm{ms}^{-1}]$ over time $t\,[\mathrm{s}]$ under the Boussinesq approximation [22, 23]:

$$\frac{\partial \mathbf{u}}{\partial t} + \mathbf{u} \cdot \nabla \mathbf{u} = \frac{1}{\rho}\left(-\nabla p + \nabla \cdot (2\mu \mathbf{D})\right) + \mathbf{g} \tag{3.1}$$

$$\nabla \cdot \mathbf{u} = 0 \tag{3.2}$$

where $\rho\,[\mathrm{kgm}^{-3}]$ is the density of air, $\mathbf{D} = \left(\nabla \mathbf{u} + (\nabla \mathbf{u})^T\right)/2\,[\mathrm{s}^{-1}]$ the deformation tensor, $\mu\,[\mathrm{Pa} \cdot \mathrm{s}]$ the dynamic viscosity of air and $\mathbf{g}$ the acceleration caused by gravity. The acceleration caused by gravity is given by the buoyancy field $b\,[\mathrm{ms}^{-2}]$ in the z-direction: $\mathbf{g} = b\hat{\mathbf{z}}\,[\mathrm{ms}^{-2}]$.
Equation 3.1 shows the Navier-Stokes equations for momentum. The first term on the left-hand side is the time-derivative of the velocity and the second term is the advection of momentum. The first term of the right-hand side is the pressure gradient, the second term the viscosity term and the last term the acceleration caused by gravity. Equation 3.2 is the continuity equation for the mass of an incompressible fluid.

For the evolution of the buoyancy field $b\,[\mathrm{ms}^{-2}]$ an advection-diffusion equation for a diffusive tracer is solved [21, 22]:

$$\frac{\partial b}{\partial t} = -\mathbf{u} \cdot \nabla b + \nabla \cdot (\kappa \nabla b) \tag{3.3}$$

where $\mathbf{u}\,[\mathrm{ms}^{-1}]$ is the velocity field and $\kappa\,[\mathrm{m}^2\mathrm{s}^{-1}]$ is the diffusivity of air. The first term on the left-hand side is the advection term and the second term the diffusive term.

The buoyancy $b\,[\mathrm{ms}^{-2}]$ is used as the thermodynamic variable of the model, the definition can be found in equation 2.1. The initial linearly stratified buoyancy profile $b(z, t = 0)\,[\mathrm{ms}^{-2}]$ of the system is given by:

$$b(z, t = 0) = N^2 z \tag{3.4}$$

where $N\,[\mathrm{s}^{-1}]$ is the Brunt-Väisälä frequency (see equation 2.3) that determines the strength of the stratification and $z\,[\mathrm{m}]$ is the height above the surface.
In figure 3.2 a visual representation of the initial background buoyancy profile is given in a $L_0\,[\mathrm{m}] \times L_0\,[\mathrm{m}]$ domain.

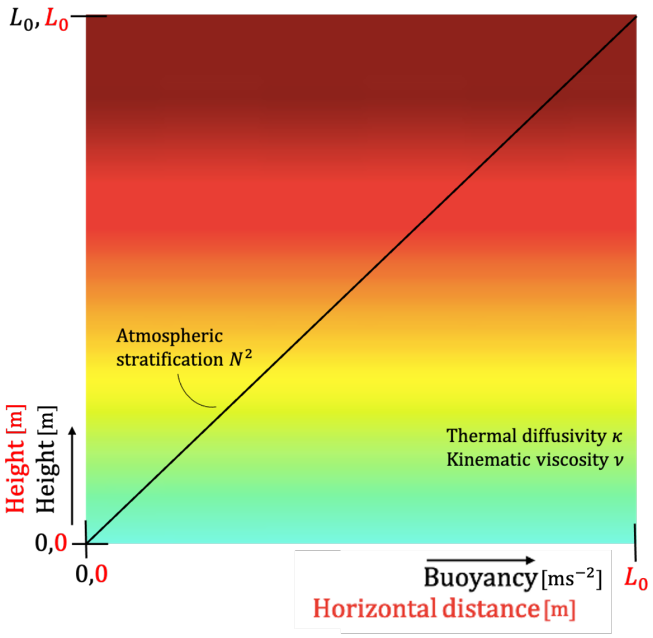

FIGURE 3.2: The initial background buoyancy field of the model and its parameters. The black axis labels belong to the black line of the buoyancy-height relation and the red labels to the colored buoyancy profile in the background. The red color of the profile belongs to the highest buoyancy values and the greenish/blue color to the lowest buoyancy values.

The following boundary conditions are implemented in the model:

- For the left ($x = 0\,\text{m}$) and the right ($x = L_0\,[\text{m}]$) side of the domain periodic boundaries for $b\,[\text{ms}^{-2}]$ are chosen.
- For the top ($z = L_0\,[\text{m}]$) boundary a Neumann boundary condition is chosen: $\frac{\partial b}{\partial z} = 0\,\text{s}^{-2}$.
- For the lower ($z = 0\,\text{m}$) boundary a typical no-slip boundary condition is chosen: $u_x = 0\,\text{ms}^{-1}$ and $u_y = 0\,\text{ms}^{-1}$ (u_y only in 3D).
- For the lower ($z = 0\,\text{m}$) boundary an additional Dirichlet boundary condition is applied to create surface buoyancy sources with strength $b_0\,[\text{ms}^{-2}]$. The exact definition of this lower boundary condition is given in the method of the case studies. The typical effect of a surface buoyancy source with strength $b_0\,[\text{ms}^{-2}]$ in a stable atmosphere is shown and explained in figure 3.3.
- In the 3D model there are two additional boundaries; the front ($y = 0\,\text{m}$) and back ($y = L_0\,[\text{m}]$) boundary. For those boundaries a periodic boundary condition for $b\,[\text{ms}^{-2}]$ is chosen.

Additionally, in a two dimensional model it is not possible to describe 3D turbulence and its dissipation (in absence of vortex stretching). In order to create artificial dissipation

of second order moments in the 2D model, a hyper-viscous $\nu\,[\mathrm{m^2 s^{-1}}]$ and hyper-diffusive $\kappa\,[\mathrm{m^2 s^{-1}}]$ atmosphere is considered (i.e. larger than the usual molecular values).

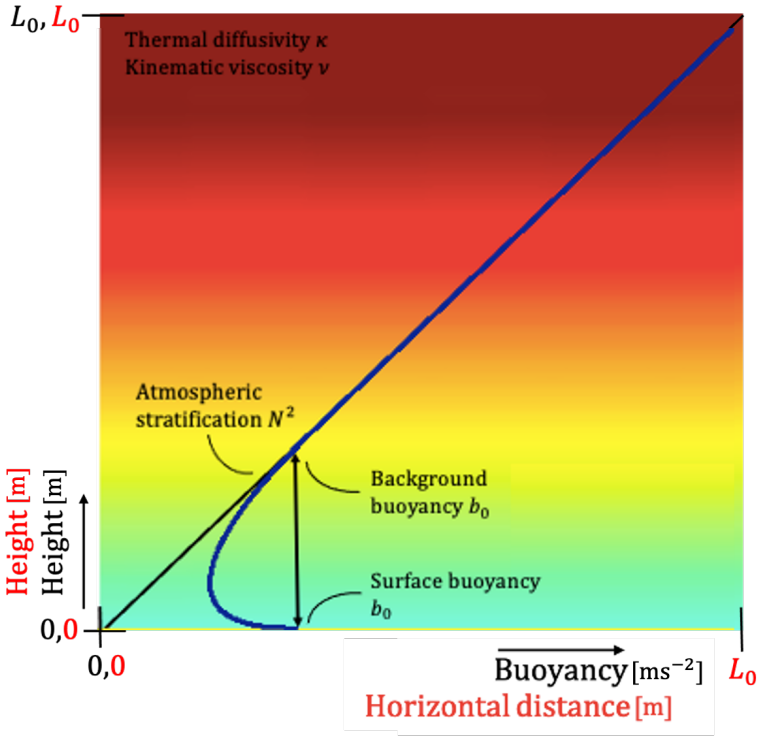

FIGURE 3.3: The initial background buoyancy field (see equation 3.4) of the system is shown in the colored buoyancy profile in the background, the red axis labels belong to this colored profile. The black line shows the initial buoyancy-height profile and the blue line shows a typical buoyancy-height profile of a stably stratified system with surface buoyancy $b_0\,[\mathrm{ms^{-2}}]$. Both lines belong to the black axis labels.

To diagnose model outcomes, additional physical quantities are calculated over time: the total kinetic energy $e\,[\mathrm{m^4 s^{-2}}]$, $[\mathrm{m^5 s^{-2}}]$ in the system, the dissipation of kinetic energy $\epsilon\,[\mathrm{m^4 s^{-3}}]$, $[\mathrm{m^5 s^{-3}}]$ and the surface flux $\Phi_{surface}\,[\mathrm{m^3 s^{-3}}]$ (units for respectively 2D, 3D):

$$e = \int \frac{1}{2}\mathbf{u}^2 dV \tag{3.5}$$

$$\epsilon = -\nu \int (\nabla \mathbf{u})^2\, dV \tag{3.6}$$

$$\Phi_{surface} = \nu \int_{surface} \left(\frac{\partial b}{\partial z}\right)\Big|_{surface} dA \tag{3.7}$$

with $V\,[\mathrm{m^2}]$ the area (2D) or $V\,[\mathrm{m^3}]$ the volume (3D) of the domain, $z\,[\mathrm{m}]$ the vertical height and $dA = dx_{z=0}\,[\mathrm{m}]$ the length (2D) or $dA = (dxdy)_{z=0}\,[\mathrm{m^2}]$ the area (3D) of the surface. The square of a vector is defined as its inner product (e.g. $\mathbf{u}^2 = \mathbf{u} \cdot \mathbf{u}$).

3.1.3 Case studies

Different case studies are performed, their contribution to answer the research question can be found in the applied strategy on page 13.
The exact implementation of the described methods are made available online:

The 2D-model (section 3.1.3.1 and 3.1.3.2):
http://basilisk.fr/sandbox/mbreedijk/surface_heterogeneity_2D.c
The 3D-model (section 3.1.3.3):
http://basilisk.fr/sandbox/mbreedijk/surface_heterogeneity_3D.c
The 2D-model with land-surface atmosphere coupling (section 3.1.3.4):
http://basilisk.fr/sandbox/mbreedijk/surface_heterogeneity_coupling.c

3.1.3.1 One heat source (2D simulation)

Firstly, to check that the model works and that the outcomes seem 'logical' with basic physical interpretation, a simple case study is carried out. The case of a single heat source at the surface in a stable boundary layer is represented in a two-dimensional model. It can be seen as an idealized 2D representation of a ditch through a flat homogeneous landscape (see figure 3.4). Since water has another thermal exchange rate compared to the rest of the homogeneous surface, it can be seen as a thermal memory of daytime heating and so it becomes a heat source during the night.

FIGURE 3.4: Ditch through (near) homogeneous meadow.

The heat source is modelled as a heaviside function with width $w\,[\mathrm{m}]$ and buoyancy amplitude $b_0\,[\mathrm{ms}^{-2}]$ at the surface ($z = 0\,\mathrm{m}$):

$$b(x)_{z=0} = \begin{cases} b_0, & \text{if } \left(\frac{L_0}{2} - \frac{w}{2}\right) < x < \left(\frac{L_0}{2} + \frac{w}{2}\right) \\ 0, & \text{otherwise} \end{cases} \tag{3.8}$$

The domain is $L_0\,[\mathrm{m}] \times L_0\,[\mathrm{m}]$ and the atmosphere has a viscosity $\nu\,[\mathrm{m}^2\mathrm{s}^{-1}]$, diffusivity $\kappa\,[\mathrm{m}^2\mathrm{s}^{-1}]$ and Brunt-Väisälä frequency $N\,[\mathrm{s}^{-1}]$ (see equation 2.3). The typical convective length scale above the source is $\mathcal{L}\,[\mathrm{m}]$ (see equation 3.11). The simulation setup with the relevant physical quantities is shown in figure 3.5.

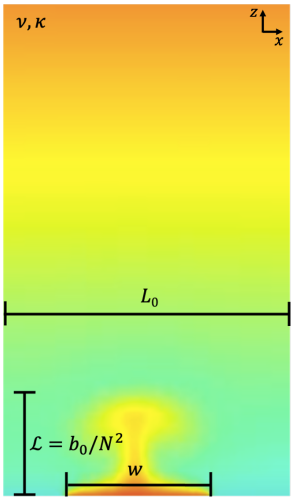

FIGURE 3.5: The buoyancy field of a two dimensional simulation of a heaviside buoyancy source at the surface in a stable boundary layer. The red color represents the highest buoyancy and the blue/green color the lowest buoyancy values.

The system is described by six parameters $\{w, L_0, b_0, N, \nu, \kappa\}$ and two base-units: length and time (l, t). So, the system results in four independent dimensionless Π-groups [16]:

$$\Pi_1 = \mathcal{L}/w = 2 \tag{3.9a}$$

$$\Pi_2 = L_0/w \tag{3.9b}$$

$$\Pi_3 = \nu/\kappa = 1 \tag{3.9c}$$

$$\Pi_4 = b_0^2/N^3\nu = 2000 \tag{3.9d}$$

The first two Π-groups give the ratio of two length scales; the convective length scale (see equation 3.11) compared to the width of the source and the length of the domain compared to the width of the source respectively. $\Pi_2\,[-]$, the dimensionless domain width, is varied in the simulations performed. $\Pi_3\,[-]$ can be compared to the Prandtl number and $\Pi_4\,[-]$ to the Reynolds number. These dimensionless Π-groups are defined to minimize the number of independent parameters.

The corresponding physical values for the six parameters are:

$$w = 1\,\mathrm{m} \tag{3.10a}$$

$$L_0 = 5 - 90\,\mathrm{m} \tag{3.10b}$$

$$b_0 = 2\,\mathrm{ms}^{-2} \tag{3.10c}$$

$$N = 1\,\mathrm{s}^{-1} \tag{3.10d}$$

$$\nu = 0.002\,\mathrm{m}^2\mathrm{s}^{-1} \tag{3.10e}$$

$$\kappa = 0.002\,\mathrm{m}^2\mathrm{s}^{-1} \tag{3.10f}$$

$L_0\,[\mathrm{m}]$ is varied in the different simulations to check the effect of the domain size (the 'walls'), while the other parameters are kept constant.

In order to scale the physical parameters of the system and to get a better physical understanding of the system, four characteristic scales (concept introduced in section 2.2.2) are defined.
First, a characteristic convective length scale $\mathcal{L}\,[\mathrm{m}]$ is defined:

$$\mathcal{L} = \frac{b_0}{N^2} \tag{3.11}$$

The length scale $\mathcal{L}\,[\mathrm{m}]$ is the height at which the buoyancy of the initial background stratification of the atmosphere (see equation 3.4) equals the surface heterogeneity buoyancy $b_0\,[\mathrm{ms}^{-2}]$. The characteristic area of the influence of the heat source is given by $\mathcal{A} = w\mathcal{L}\,[\mathrm{m}^2]$.

Secondly, a characteristic velocity scale $\mathcal{U}\,[\mathrm{ms}^{-1}]$ is defined:

$$\mathcal{U} = \frac{b_0}{N} \tag{3.12}$$

Finally, a characteristic buoyancy scale $\mathcal{B}\,[\mathrm{ms}^{-2}]$ is defined:

$$\mathcal{B} = b_0 \tag{3.13}$$

The Reynolds number Π_4 can now be rewritten to the classical definition $\mathrm{Re} = \Pi_4 = \mathcal{U}\mathcal{L}/\nu$.

The physical quantities $e, \epsilon, \Phi_{surface}$ are scaled by the typical scales and studied as dimensionless parameters $e^*, \epsilon^*, \Phi^*_{surface}$ in the results:

$$e^* = \frac{1}{\mathcal{U}^2\mathcal{A}}e = \frac{N^2}{b_0^2 w\mathcal{L}}e \tag{3.14}$$

$$\epsilon^* = \frac{\mathcal{L}^2}{\nu\mathcal{U}^2\mathcal{A}}\epsilon = \frac{1}{\nu b_0 w}\epsilon \tag{3.15}$$

$$\Phi^*_{surface} = \frac{1}{\nu\mathcal{B}}\Phi_{surface} = \frac{1}{\nu b_0}\Phi_{surface} \tag{3.16}$$

Additionally, the dimensionless asymptotic values (i.e. steady state values) of the parameters $e^*_{asymp}, \epsilon^*_{asymp}, \Phi^*_{asymp}\,[-]$ are also used in the results. The asymptotic values of the parameters are always an average of the last 20 time steps (the last 25 seconds) calculated under the condition that the parameter does not vary more than 8% over those time steps. The goal is to find relations between these parameters and the dimensionless groups.

3.1.3.2 Multiple heat sources (2D simulation)

To look at the effect of the spatial distribution of surface heterogeneities on the mixing, a case study on two identical heaviside heat sources with width $w\,[\mathrm{m}]$ and strength

$b_0\,[\mathrm{ms}^{-2}]$ at the surface ($z = 0\,\mathrm{m}$) a distance $d\,[\mathrm{m}]$ apart is performed:

$$b(x)_{z=0} = \begin{cases} b_0, & \text{if } \left(\frac{L_0}{2} - \frac{d}{2} - \frac{w}{2}\right) < x < \left(\frac{L_0}{2} - \frac{d}{2} + \frac{w}{2}\right) \\ b_0, & \text{if } \left(\frac{L_0}{2} + \frac{d}{2} - \frac{w}{2}\right) < x < \left(\frac{L_0}{2} + \frac{d}{2} + \frac{w}{2}\right) \\ 0, & \text{otherwise} \end{cases} \tag{3.17}$$

The setup with the relevant physical quantities is shown in figure 3.6, the definition of the parameters is explained in section 3.1.3.1.

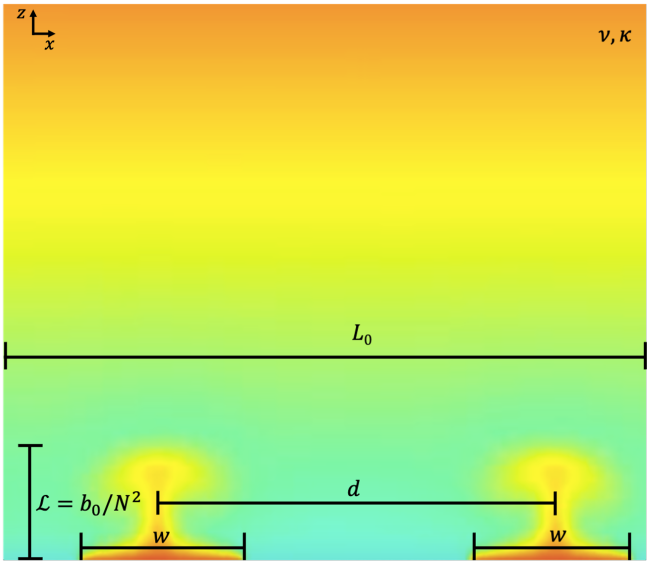

FIGURE 3.6: The buoyancy field of a two dimensional simulation of two heaviside buoyancy sources at the surface in a stable boundary layer. The red color represents the highest buoyancy and the blue/green color the lowest buoyancy values.

The system is described by seven parameters $\{w, d, L_0, b_0, N, \nu, \kappa\}$ and two base-units: length and time (l, t). So, the system results in five independent dimensionless Π-groups [16]:

$$\Pi_1 = \mathcal{L}/w = 2 \tag{3.18a}$$

$$\Pi_2 = (L_0 - d)/2w = 60 \tag{3.18b}$$

$$\Pi_3 = \nu/\kappa = 1 \tag{3.18c}$$

$$\Pi_4 = b_0^2/N^3\nu = 2000 \tag{3.18d}$$

$$\Pi_5 = d/w \tag{3.18e}$$

The first two Π-groups give the ratio of two length scales; the convective length scale compared to the width of the source and the distance between the sources and the end of the domain $(L_0 - d)$ compared to the total width of the two sources $(2w)$ respectively. The motivation to choose this definition for Π_2 can be found in equation 4.2. $\Pi_3\,[-]$ can be compared to the Prandtl number and $\Pi_4\,[-]$ to the Reynolds number. $\Pi_5\,[-]$ is again

the ratio of two length scales; the distance between the sources and the width of one source, this value is varied in the different simulations.

The corresponding physical values for the seven parameters are:

$$w = 0.5\,\mathrm{m} \tag{3.19a}$$
$$d = 0.5 - 15\,\mathrm{m} \tag{3.19b}$$
$$L_0 = 60.5 - 75\,\mathrm{m} \tag{3.19c}$$
$$b_0 = 1\,\mathrm{ms}^{-2} \tag{3.19d}$$
$$N = 1\,\mathrm{s}^{-1} \tag{3.19e}$$
$$\nu = 0.002\,\mathrm{m}^2\mathrm{s}^{-1} \tag{3.19f}$$
$$\kappa = 0.002\,\mathrm{m}^2\mathrm{s}^{-1} \tag{3.19g}$$

$d\,[\mathrm{m}]$ (and subsequently $L_0\,[\mathrm{m}]$) is varied in the different simulations to study the effect of the distance between the sources, while the other parameters are kept constant.

In this case study, the same characteristic scales and dimensionless parameters can be used as in section 3.1.3.1. The asymptotic values of the parameters $e^*_{asymp}, \epsilon^*_{asymp}, \Phi^*_{asymp}\,[-]$ are also defined in the same way as described in section 3.1.3.1.

3.1.3.3 Multiple heat sources (3D simulation)

The described model of section 3.1.3.2 is extended to a three-dimensional model. This means that the flow may generate 3D turbulence, such that i.e. vortex stretching is modelled, as is the case in reality.

Again, two identical heaviside heat sources with amplitude $b_0\,[\mathrm{ms}^{-2}]$ a distance $d\,[\mathrm{m}]$ apart at the surface ($z = 0\,\mathrm{m}$) are modelled, but now in a 3D domain $L_0\,[\mathrm{m}] \times L_0\,[\mathrm{m}] \times L_0\,[\mathrm{m}]$:

$$b(x,y)_{z=0} = \begin{cases} b_0, & \text{if } \left(\frac{L_0}{2} - \frac{d}{2} - \frac{w}{2}\right) < x < \left(\frac{L_0}{2} - \frac{d}{2} + \frac{w}{2}\right), \forall y \in [0, L_0] \\ b_0, & \text{if } \left(\frac{L_0}{2} + \frac{d}{2} - \frac{w}{2}\right) < x < \left(\frac{L_0}{2} + \frac{d}{2} + \frac{w}{2}\right), \forall y \in [0, L_0] \\ 0, & \text{otherwise} \end{cases} \tag{3.20}$$

This surface buoyancy is chosen to let it resemble the situation of two ditches through a 'homogeneous' meadow (see figure 3.4). The initial ($t = 0\,\mathrm{s}$) buoyancy magnitude at the surface with the relevant physical quantities is shown in figure 3.7, the parameters are explained in section 3.1.3.1. The background buoyancy is identical to the profile in 2D (see figure 3.2) extended homogeneously for the y-direction.

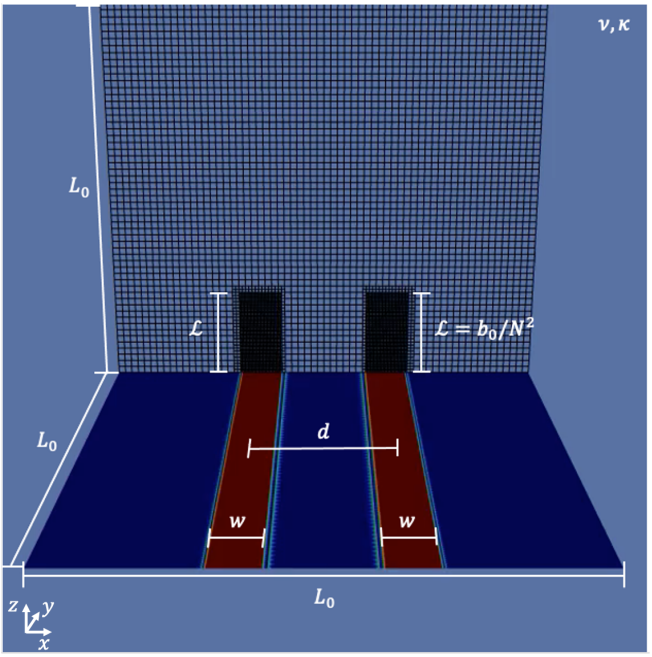

FIGURE 3.7: The initial setup of the three dimensional simulation of two heaviside buoyancy sources with length $L_0\,[\mathrm{m}]$ at the surface. The red color of the surface represents the strength of the sources $b_0\,[\mathrm{ms}^{-2}]$ and the surface with the blue color has a buoyancy equal to zero ($b = 0\,\mathrm{ms}^{-2}$).

The system is described by seven parameters $\{w, d, L_0, b_0, N, \nu, \kappa\}$ and two base-units: length and time (l, t). So, the system results in five independent dimensionless Π-groups [16]:

$$\Pi_1 = \mathcal{L}/w = 2 \tag{3.21a}$$

$$\Pi_2 = L_0/w = 130 \tag{3.21b}$$

$$\Pi_3 = \nu/\kappa = 1 \tag{3.21c}$$

$$\Pi_4 = b_0^2/N^3\nu = 20000 \tag{3.21d}$$

$$\Pi_5 = d/w \tag{3.21e}$$

The first two Π-groups give the ratio of two length scales; the convective length scale compared to the width of the source and the domain size compared to the width of the sources respectively. $\Pi_3\,[-]$ can be compared to the Prandtl number and $\Pi_4\,[-]$ to the Reynolds number. $\Pi_5\,[-]$ is again the ration of two length scales; the distance between the sources and the width of the sources. To see the effect of the distance between the sources on the outcomes, $\Pi_5\,[-]$ is varied.

The corresponding physical values for the seven parameters are:

$$w = 0.5\,\mathrm{m} \tag{3.22a}$$

$$d = 0.5 - 16\,\mathrm{m} \tag{3.22b}$$

$$L_0 = 65\,\mathrm{m} \tag{3.22c}$$

$$b_0 = 1\,\mathrm{ms}^{-2} \tag{3.22d}$$

$$N = 1\,\mathrm{s}^{-1} \tag{3.22e}$$

$$\nu = 5.0 \cdot 10^{-5}\,\mathrm{m}^2\mathrm{s}^{-1} \tag{3.22f}$$

$$\kappa = 5.0 \cdot 10^{-5}\,\mathrm{m}^2\mathrm{s}^{-1} \tag{3.22g}$$

$d\,[\mathrm{m}]$ is varied in the different simulations to study the effect of the distance between the sources, while the other parameters are kept constant.

In this case study, the same characteristic scales can be used as in section 3.1.3.1. An additional characteristic scale for the volume of the influence of the heat source is given by $\mathcal{V} = w\mathcal{L}L_0\,[\mathrm{m}^3]$.

The physical quantities $e, \epsilon, \Phi_{surface}$ are again studied as dimensionless parameters $e^*, \epsilon^*, \Phi^*_{surface}$. They are now defined by:

$$e^* = \frac{1}{\mathcal{U}^2\mathcal{V}}e = \frac{N^2}{b_0^2 w\mathcal{L}L_0}e \tag{3.23}$$

$$\epsilon^* = \frac{\mathcal{L}^2}{\nu\mathcal{U}^2\mathcal{V}}\epsilon = \frac{1}{\nu b_0 w L_0}\epsilon \tag{3.24}$$

$$\Phi^*_{surface} = \frac{1}{\nu\mathcal{B}}\Phi_{surface} = \frac{1}{\nu b_0}\Phi_{surface} \tag{3.25}$$

The asymptotic values of the parameters $e^*_{asymp}, \epsilon^*_{asymp}, \Phi^*_{asymp}\,[-]$ are again studied in the results and are defined in the same way as in section 3.1.3.1.

3.1.3.4 The effect of surface-atmosphere coupling (2D simulation)

This part presents a rudimentary model, inspired by previous research [25], to implement surface-atmosphere coupling in studying surface heterogeneity. The results will only show that the outcomes are in correspondence with the previous case studies and with basic physical interpretation. No further research into the effect of the spatial distribution of surface heterogeneity is conducted.
In the previous simulation setups the surface buoyancy is kept constant over time. In reality, this surface buoyancy itself changes during nights. Surface temperature (and hence buoyancy) will change by radiative cooling, turbulent heat transfer and soil heat conduction, as displayed in the surface energy budget (SEB) (see equation 2.4). Because simplicity of the model is desired, a simplified version of the SEB is introduced [25]. The

net radiation (R_n), the soil heat flux (F) and the sensible heat flux (H) of equation 2.4 are considered:

$$R_n = F + H \tag{3.26}$$

R_n [Wm^{-2}] is positive if the flux is directed towards the surface, F [Wm^{-2}] and H [Wm^{-2}] are positive if the flux is directed away from the surface.

In this model the buoyancy b [ms^{-2}] is used as the thermodynamic variable (see equation 2.1). The fluxes of equation 3.26 can also be expressed by their buoyancy equivalents; the net buoyancy radiation (R^*), the soil buoyancy flux (G) and the sensible buoyancy flux (B) by dividing them by a factor $\theta_{ref}\rho C_p g^{-1}$:

$$R^* = G + B \tag{3.27}$$

where θ_{ref} [K] is a constant reference potential temperature, ρ [kgm^{-3}] is the air density, C_p [$\mathrm{J(kgK)}^{-1}$] is the heat capacity of air at constant pressure and g [ms^{-2}] is the gravitational constant.

The net buoyancy radiation R^* [$\mathrm{m}^2\mathrm{s}^{-3}$] is prescribed to the model and is taken constant over time during the simulation, which can be roughly justified by observations during stably stratified nights in Cabauw [25].

The soil buoyancy flux G [$\mathrm{m}^2\mathrm{s}^{-3}$] is described by a 'lumped-parameter feedback' [25, 26]. In this concept two parameters are used to prescribe the negative feedback of the surface buoyancy b_{surf} [ms^{-2}] using an effective feedback-buoyancy b_d [ms^{-2}] and an effective coupling strength Λ [ms^{-1}]:

$$G = \Lambda(b_{surf} - b_d) \tag{3.28}$$

This coupling is caused by a combination of radiation and conduction processes in the atmosphere and the soil. The effective feedback-buoyancy b_d [ms^{-2}] can be seen as the buoyancy at depth d [m] that does not change over time. This 'lumped-parameter concept' is an idealized way of describing the soil heat flux. In reality, various properties of the soil (e.g. water content and spatial temperature variation in soil) and the temporal heat storage effects determine the soil buoyancy flux G [$\mathrm{m}^2\mathrm{s}^{-3}$] as a function of the surface buoyancy. However, in previous research [25, 26] it is shown that the concept shows some degree of realism, especially during nights.

The sensible buoyancy flux at the surface B [$\mathrm{m}^2\mathrm{s}^{-3}$] is defined as:

$$B = \kappa \left.\frac{\partial b}{\partial z}\right|_{surface} \tag{3.29}$$

where κ [$\mathrm{m}^2\mathrm{s}^{-1}$] is the diffusivity and $\left.\frac{\partial b}{\partial z}\right|_{surface}$ [ms^{-1}] the derivative of buoyancy with height at the surface.

From equations 3.27, 3.28 and 3.29 a Robin boundary condition for the soil surface buoyancy can be deduced:

$$\Lambda b_{surf} + \kappa \frac{\partial b}{\partial \mathbf{n}}\bigg|_{surf} = R^* + \Lambda b_d \tag{3.30}$$

This condition expresses both the surface value of buoyancy and its derivative in terms of known present values. The Robin condition can be viewed as a generalisation of Neumann and Dirichlet conditions.

The initial stratification of the system $b(t=0,z)\,[\mathrm{ms}^{-2}]$ is defined as:

$$b(t=0,z) = b_{(z=0)} + N^2 z \tag{3.31}$$

where $N\,[\mathrm{s}^{-1}]$ is the Brunt-Väisälä frequency, $z\,[\mathrm{m}]$ is the distance above the surface and $b_{(z=0)}\,[\mathrm{ms}^{-2}]$ is the initial buoyancy of the surface. The initial buoyancy of the surface $b_{(z=0)}\,[\mathrm{ms}^{-2}]$ is defined by a heaviside function with two peaks with width $w\,[\mathrm{m}]$ a distance $d\,[\mathrm{m}]$ apart with buoyancy amplitude $b_0\,[\mathrm{ms}^{-2}]$ (see equation 3.17). This is a simplified way to resemble the temperature differences because of surface heterogeneity at the beginning of the night. The soil buoyancy flux varies for different types of surface: strong coupling for the heat sources with $\Lambda_w\,[\mathrm{ms}^{-1}]$ and weak coupling for the 'colder' remainder of the domain with $\Lambda_s\,[\mathrm{ms}^{-1}]$.

The setup with the relevant physical quantities are shown in figure 3.8.

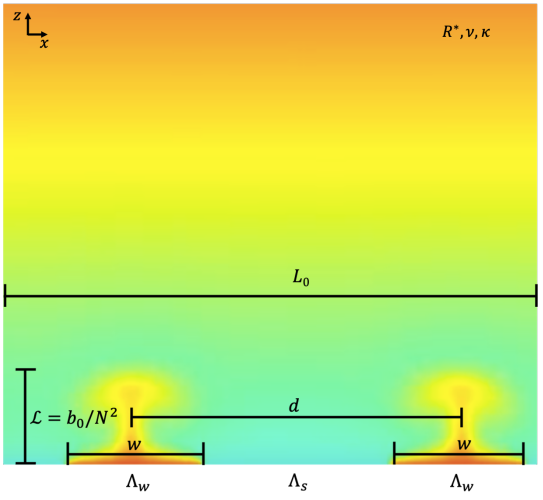

FIGURE 3.8: The buoyancy field of a two dimensional simulation of two heaviside buoyancy sources at the surface in a stable boundary layer with surface atmosphere-feedback. The red color represents the highest buoyancy and the blue/green color the lowest buoyancy values.

The system is described by 10 parameters $\{w, d, L_0, b_0, N, \nu, \kappa, \Lambda_w, \Lambda_s, R^*\}$ and two base-units: length en time (l, t). So, the system results in eight independent dimensionless

Π-groups [16]:

$$\Pi_1 = \mathcal{L}/w = 2 \tag{3.32a}$$
$$\Pi_2 = L_0/w = 20 \tag{3.32b}$$
$$\Pi_3 = \nu/\kappa = 1 \tag{3.32c}$$
$$\Pi_4 = b_0^2/N^3\nu = 2000 \tag{3.32d}$$
$$\Pi_5 = d/w = 4 \tag{3.32e}$$
$$\Pi_6 = \Lambda_w/\Lambda_s = 10 \tag{3.32f}$$
$$\Pi_7 = R^*/b_0 = -0.012 \tag{3.32g}$$
$$\Pi_8 = \Lambda_w/Nw = 0.0012 \tag{3.32h}$$

The first two Π-groups give the ratio of two length scales; the convective length scale compared to the width of the source and the domain size compared to the width of the sources respectively. $\Pi_3\,[-]$ can be compared to the Prandtl number and $\Pi_4\,[-]$ to the Reynolds number. $\Pi_5\,[-]$ is again the ration of two length scales; the distance between the sources and the width of the sources. $\Pi_6\,[-]$ give the ratio of the lumped parameter of the heat sources compared to the lumped parameter of the rest of the surface. $\Pi_7\,[-]$ gives the ratio of two buoyancy scales of the model and $\Pi_8\,[-]$ of two velocity scales.

The corresponding physical values for the ten parameters are:

$$w = 0.5\,\mathrm{m} \tag{3.33a}$$
$$d = 2\,\mathrm{m} \tag{3.33b}$$
$$L_0 = 10\,\mathrm{m} \tag{3.33c}$$
$$b_0 = 1\,\mathrm{ms}^{-2} \tag{3.33d}$$
$$N = 1\,\mathrm{s}^{-1} \tag{3.33e}$$
$$\nu = 0.0005\,\mathrm{m}^2\mathrm{s}^{-1} \tag{3.33f}$$
$$\kappa = 0.0005\,\mathrm{m}^2\mathrm{s}^{-1} \tag{3.33g}$$
$$\Lambda_w = 0.006\,\mathrm{ms}^{-1} \tag{3.33h}$$
$$\Lambda_s = 0.0006\,\mathrm{ms}^{-1} \tag{3.33i}$$
$$R^* = -0.012\,\mathrm{m}^2\mathrm{s}^{-3} \tag{3.33j}$$

The parameter values are inspired by some observational analysis performed in previous research [25], but detailed substantiation and comparison with reality is lacking. The total kinetic energy $e\,[\mathrm{m}^4\mathrm{s}^{-2}]$ (see equation 3.5), the dissipation of the kinetic energy $\epsilon\,[\mathrm{m}^4\mathrm{s}^{-3}]$ (see equation 3.6) and the surface flux $\Phi_{surface}\,[\mathrm{m}^3\mathrm{s}^{-2}]$ (see equation 3.7) are studied over time.

3.2 Field experimental method

To be able to make a quantitative comparison between the simulations and the real-life effect of surface heterogeneity a field experiment is performed. Inspired by previous research [27, 28], a screen with an infrared camera pointing at it is used to capture the temperature flow above surface heterogeneity.

The thermal measurements are conducted by an infrared camera Optris PI 400i/PI 450i with an optical resolution of 382 x 288 pixels, a thermal sensitivity of 40 mK and a temperature range of −20 °C up to 900 °C [29].

An infrared camera is not able to visualize air temperatures, so a solid surface that represents this 'air temperature' is necessary to make a visualization. In order to select a suitable material for this use, the material has to meet four criteria:

- The material is highly thermally reactive and sensitive to the air temperature and thus has a low heat capacity.
- The material has a high emissivity, so that the infrared camera can capture its temperature.
- The material is water repellent.
- The material can be stretched to get a smooth surface at the installation.

Testing of various materials in previous research [27] concluded that a polyester cloth with polyacrylate cover (commonly used as anti-slip mat) is best suitable. Research [27, 28] showed that a setup with this cloth can capture microscale flows. The results show compatibility to the results of traditional methods (e.g. temperature sensors), while spatial coherence in the measurements is achieved. Because of this conclusion, our setup is based on this setup [27]. The emissivity of this material is 0.94 [−]. The 'air temperatures' shown in the results are the measured screen temperatures adjusted by this emissivity:

$$T_{air} = \left(\frac{T_{screen}^4}{0.94} \right)^{1/4} \tag{3.34}$$

where T_{air} [K] is the calculated 'air temperature', it is the temperature of the screen measured by the infrared camera T_{screen} [K] corrected by the emissivity of 0.94 [−]. Atmospheric absorption is neglected, because the distance between the camera and the camera is relatively small.

The screen is mounted between a construction of three wooden poles. The poles are placed into the ground and the total construction is secured with guy wires and pegs to prevent movement of the screen. The infrared camera is directed towards the screen at 2.5 m from the screen. The schematic setup is shown in figure 3.9.

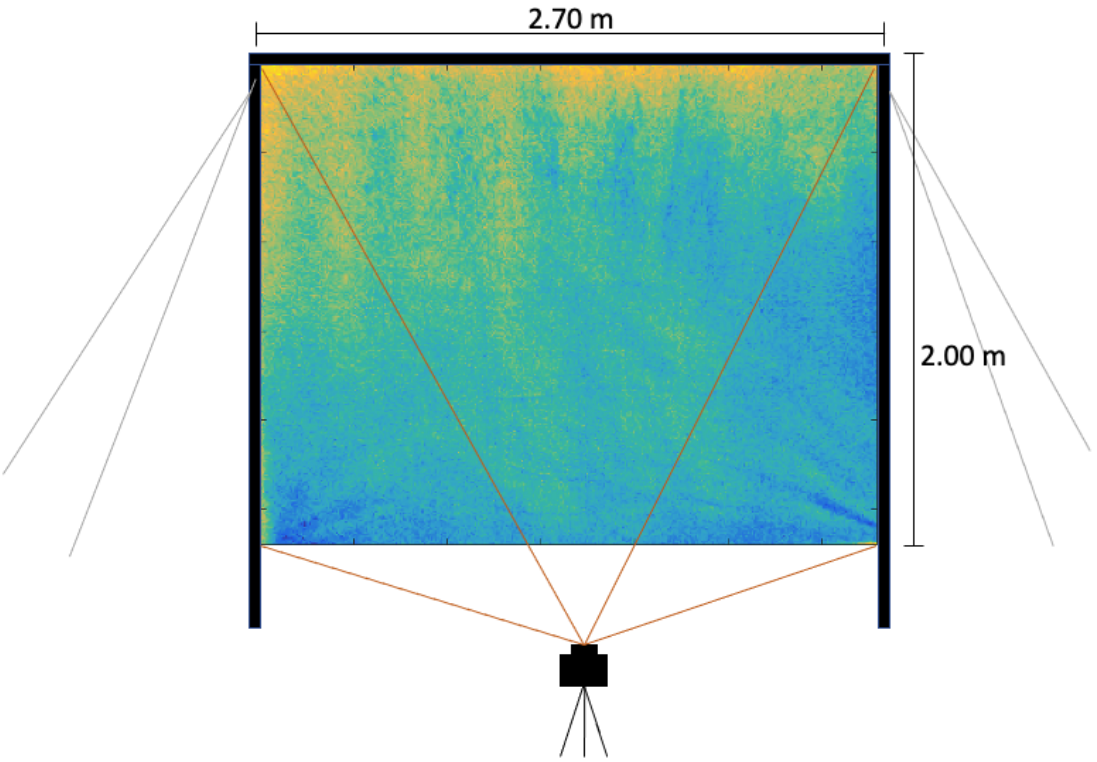

FIGURE 3.9: A schematic overview of the setup of the screen and the IR-camera.

The measurements are performed on a pear orchard (Vogelaar Fruitcultures [30]) in Krabbendijke (Zeeland, The Netherlands, 51°25'44.7"N, 4°48'8.5"E). The measurements took place in the night between April 13th and April 14th, 2021. The local weather conditions during this night were low winds ($u_{average} = 1\,\mathrm{ms}^{-1}, u_{gust} = 2\,\mathrm{ms}^{-1}$) and mainly clear skies with some cirrus clouds. As a result a strong stratification developed.

During measurement the camera took snapshots of the temperature with a frequency of 0.1 Hz. From those snapshots two dimensional profiles of the 'air temperature' are constructed. The experiment is conducted in two parts: one part above a natural surface heterogeneity and the other part above artificial surface heterogeneities.

3.2.1 Experiment above natural surface heterogeneity

The goal of this part of the experiment is to capture the flow above a natural heat source. This can be used to verify the flow pattern of the simulations. At the measuring site a real natural surface heterogeneity was not present, therefore a steel road plate on top of bare soil was used as surface heterogeneity. The screen is placed above the road plate, as shown in figure 3.10. Steel and bare soil effectively store heat during the day due to a relatively high thermal conductivity. The steel and bare soil surface are thus expected to act as a thermal heat source during the night.

FIGURE 3.10: The setup of the screen placed above a steel road plate on top of bare soil.

3.2.2 Experiment above artificial surface heterogeneity

To mimic the situation of the performed simulations and look into the effect of the spatial distribution of heat sources, also an experiment with two artificial heat sources is performed. A smaller (25 x 20 x 14 cm) and a larger box (35 x 25 x 17 cm) filled with 5 cm of hot water are placed under the screen. The front side of the boxes are sprayed with paint with a high emissivity (LabIR paint [31]) to be able to measure their temperature accurately. The temperature of the boxes vary over time because of cooling, the temperature varies between the initial temperature $T_{initial} = 40.8\,°\text{C}$ and the final temperature $T_{final} = 33.0\,°\text{C}$. In figure B.4 the temperature time-series of the heat sources is displayed. First, the boxes are put close together at a distance $d = 0.5\,\text{m}$ between the center of the boxes. Secondly, the boxes are put further apart at a distance $d = 1.2\,\text{m}$. The goal of this experiment is to explore the interaction between two heat sources at different distances. The results can be compared to the results of the 3D simulation of multiple heat sources (see section 3.1.3.3) and can be used to validate this simulation.

FIGURE 3.11: The setup of the screen placed above a 'homogeneous' meadow. During the experiment the two boxes are placed directly under the screen.

Chapter 4

Results and discussion

4.1 Results of the simulation

Before the results of the case studies are presented, we need to note that a pre-study is carried out to find the 'optimal' numerical grid by testing all the adaptive parameters (see section 3.1.1). The results of the 'convergence study' can be found in Appendix A.1.

4.1.1 One heat source (2D simulation)

The main goal of this case study was to validate the designed model for a simple configuration and to show that the results appear to be physically consistent.

First, a buoyancy source of strength $b_0 = 2\,\mathrm{ms}^{-2}$ and width $w = 1\,\mathrm{m}$ is studied with the setup described in section 3.1.3.1. To make a physical interpretation of the results movies of the kinetic energy and the buoyancy level are made. Besides, a movie of the level of grid refinement is made. In figure 4.1 a snapshot of the last time step of the movies ($t = 100\,\mathrm{s}$) is shown. The figures represent the 'steady state' of the system: from analysis it appears that the flow structures do not change anymore after $t \approx 50\,\mathrm{s}$. Figure 4.2 shows the time series of the physical parameters. From that figure it is confirmed that indeed a 'steady state' is reached after $t \approx 50\,\mathrm{s}$.

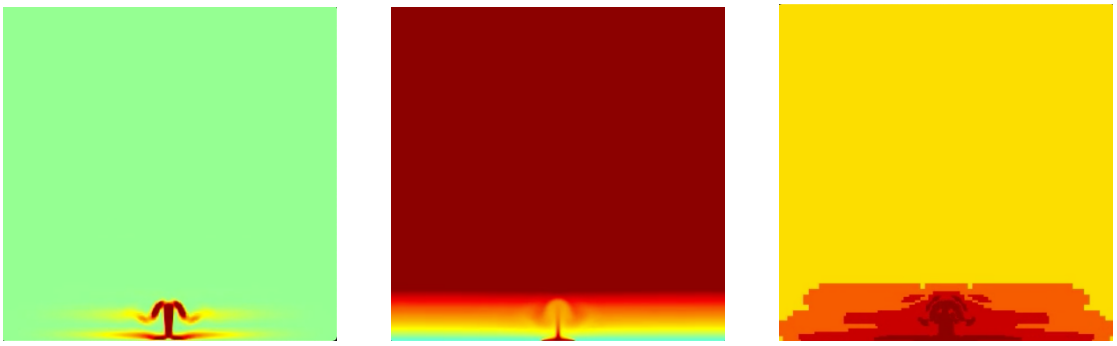

(A) The kinetic energy. (B) The buoyancy. (C) Level of grid refinement.

FIGURE 4.1: A spatial overview of three different parameters in the domain ($L_0 = 10\,\mathrm{m}$). The colors represent the magnitude of this parameter. The red color corresponds to the highest value and the green/blue color to the lowest value.

The buoyancy field shows a clear buoyancy plume above the surface heterogeneity (see also figure 3.5). The plume results from warmer air rising upward until it reaches a height where the density of the surrounding air is no longer higher and thus no buoyancy force is exerted anymore. Next, the heat plume disperses and is curled down in eddies. The eddies in the head of the plume eventually dissipate. Besides, it is noticeable that grid refining occurs in the region where indeed turbulent activity is initiated.

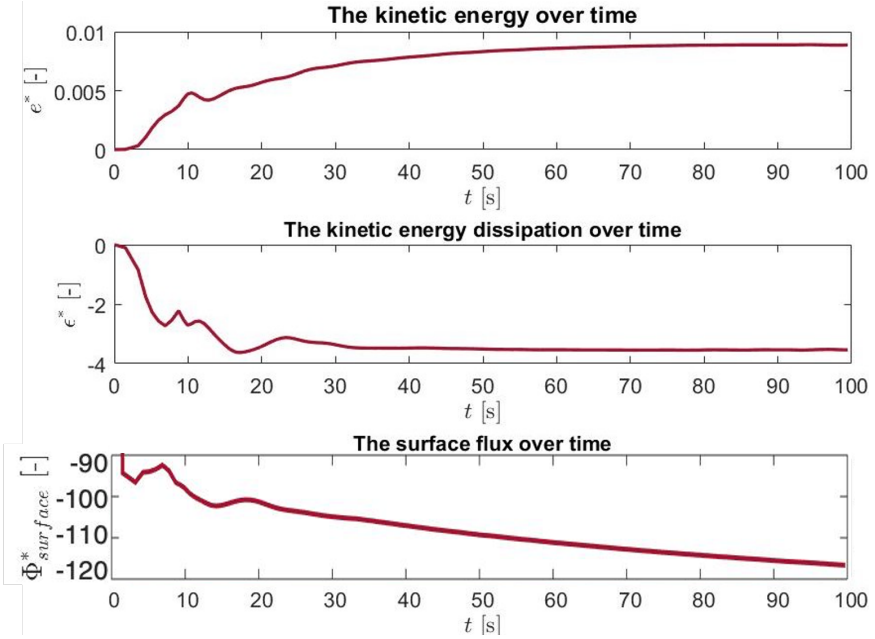

FIGURE 4.2: The evolution of the total dimensionless kinetic energy e^*, kinetic energy dissipation ϵ^* and surface flux $\Phi^*_{surface}$ of the source in domain $L_0 = 70\,\mathrm{m}$.

The buoyancy-height profile is also visualised for different time steps in figure 4.3. The buoyancy at $z/L_0\,[-]$ is the buoyancy at that height averaged over the full horizontal domain. Domain averaged, a stable stratification ($db/dz > 0\,\mathrm{s}^{-2}$) is found near the ground ($0.01 < z/L_0 < 0.1$). However, *locally* above the heat source the profile is unstable over a

depth of approximately $\mathcal{L} = b_0/N^2$ [m]. This is an example of how averaging for large scale models can give a wrong impression of *local* circumstances. This could be solved by plotting conditional profiles that distinguish the profile over and outside of the heat source.

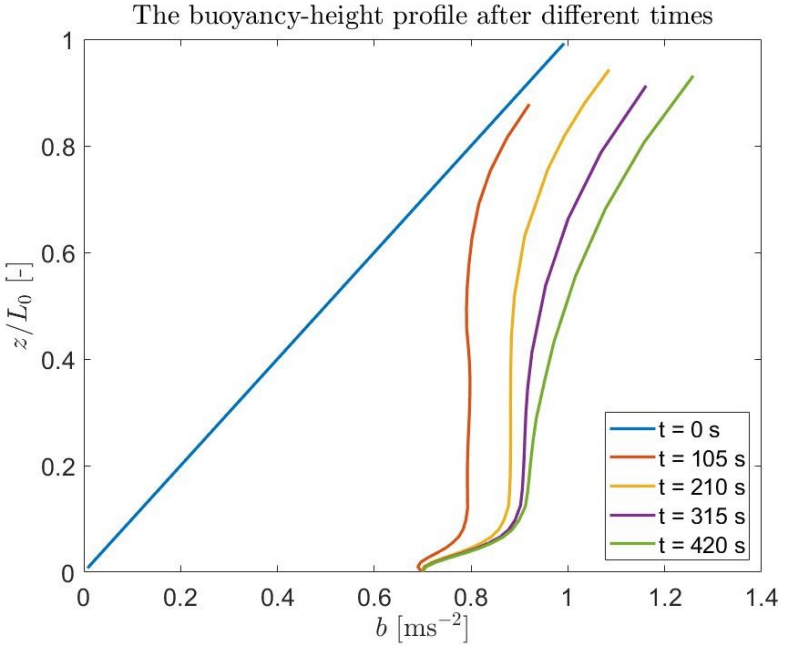

FIGURE 4.3: The buoyancy-height profile for different time steps of the source in domain $L_0 = 70\,\text{m}$.

The effect of the left and right boundary ('walls') needs to be eliminated, since there are also no 'walls' present in reality. To quantify the effect of the 'walls', the simulation is executed for various domains L_0 [m] and thus various values of $\Pi_2 = L_0/w$ [−]. The outcomes for the asymptotic (steady state) kinetic energy e^*_{asymp} [−] for different values of Π_2 [−] are shown in figure 4.4. It can be seen that starting at $L_0 \approx 60\,\text{m}$ the increase of kinetic energy with domain size saturates, with only 6% change in the range $L_0 = 60 - 90\,\text{m}$.

To verify the assumption that at $\Pi_2 \approx 60$ [−] the effect of the boundaries becomes negligible small (preferable $< 5\%$), a buoyancy source with a two times smaller strength $b_0 = 1\,\text{ms}^{-2}$ and two times smaller width $w = 0.5\,\text{m}$ is studied. In figure 4.5 the results are shown. Again, no unambiguous positive relation can be seen starting at $\Pi_2 \approx 60$ [−]. However, even for large domains e^*_{asymp} [−] varies with 15%. Therefore in the interpretation of the following results, similar variation with domain size is expected.

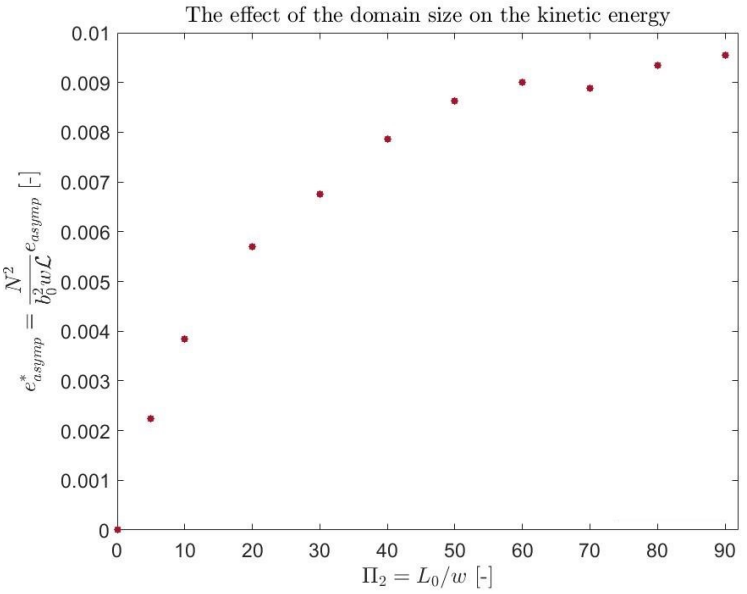

FIGURE 4.4: The effect of the domain size L_0 [m] on the asymptotic kinetic energy e^*_{asymp} [−] for a source with strength $b_0 = 2\,\mathrm{ms}^{-2}$ and width $w = 1\,\mathrm{m}$.

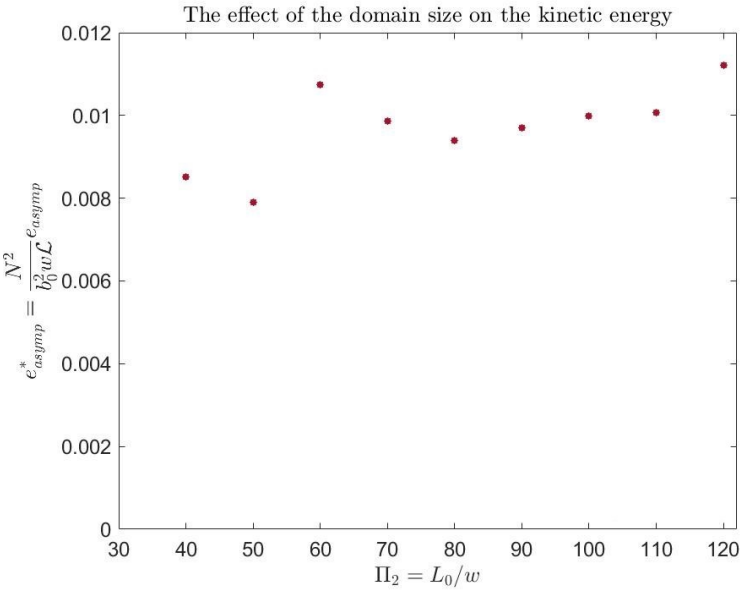

FIGURE 4.5: The effect of the domain size L_0 [m] on the asymptotic kinetic energy e^*_{asymp} [−] for a source with strength $b_0 = 1\,\mathrm{ms}^{-2}$ and width $w = 0.5\,\mathrm{m}$.

To conclude: the model seems suitable to use for further study into surface heterogeneity, but some variation in the results is expected due to natural variability within the system. This needs to be kept in mind when drawing conclusions.

4.1.2 Multiple heat sources (2D simulation)

The main goal of this case study is to look into the impact of the distance between the heterogeneities on the mixing in a stable boundary layer.

Two buoyancy sources with strength $b_0 = 1\,\mathrm{ms}^{-2}$ and width $w = 0.5\,\mathrm{m}$ and different distances $d\,[\mathrm{m}]$ between the sources are studied with the setup described in section 3.1.3.2. To make a physical interpretation of the results movies of the kinetic energy and the buoyancy field are made. Besides, a movie of the level of grid refinement is made. In figure 4.6 and 4.7 snapshots of the last time step of the movies ($t = 150\,\mathrm{s}$) are shown. The figures represent the 'steady state' of the system: from analysis it appears that the flow structures do not change anymore after $t \approx 50\,\mathrm{s}$.

In figure 4.6 the sources are a distance $d = 1\,\mathrm{m}$ apart. In figure 4.6a it is clear that the heat of the two sources attract each other and bend towards the middle forming a single heat plume. This is a surprising and non-trivial result. Likewise, in figure 4.6b the kinetic energy of the two sources show a pattern similar to that of a single source (see figure 4.1a). It seems like the distance between the sources is small enough such that the sources merge and act like a single source.

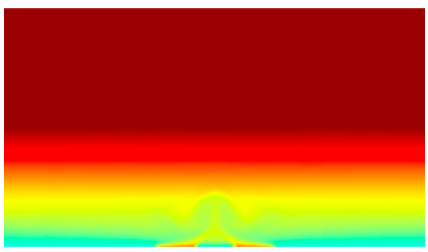

(A) The buoyancy.

(B) The kinetic energy.

(C) Level of refinement.

FIGURE 4.6: A spatial overview of three different parameters in the domain. Two sources with width $w = 0.5\,\mathrm{m}$ and strength $b_0 = 1\,\mathrm{ms}^{-2}$ a distance $d = 1\,\mathrm{m}$ apart are modelled in these figures. The figures do not show the entire domain ($L_0 = 61\,\mathrm{m}$), but a close up of the activity near the sources. The colors represent the magnitude of its parameter. The red color corresponds to the highest value and the green/blue color the lowest value.

In figure 4.7 the sources are a distance $d = 8\,\mathrm{m}$ apart. The plumes do still attract each other and bend towards each other (see figure 4.7b), but they do not merge. They act like two individual sources.

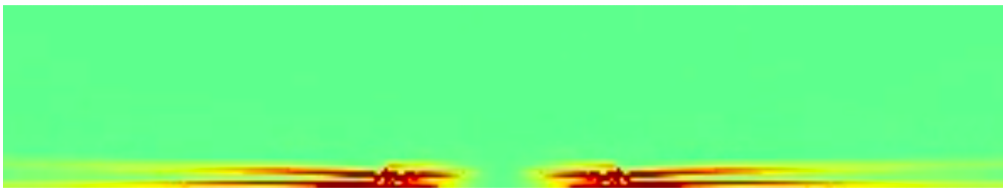

(A) The kinetic energy.

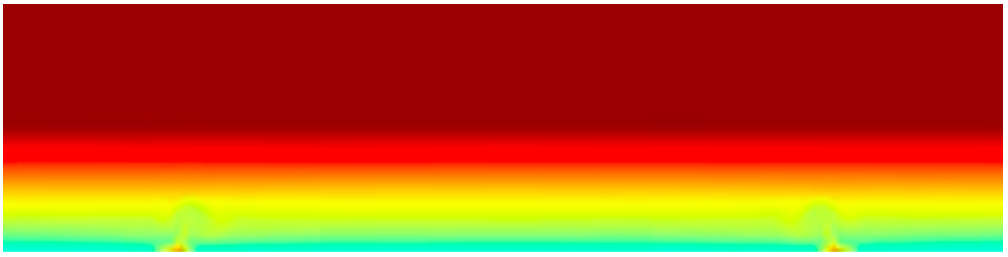

(B) The buoyancy.

(C) Level of refinement.

FIGURE 4.7: A spatial overview of three different parameters in the domain. Two sources with width $w = 0.5\,\text{m}$ and strength $b_0 = 1\,\text{ms}^{-2}$ a distance $d = 8\,\text{m}$ apart are modelled in these figures. The figures do not show the entire domain ($L_0 = 68\,\text{m}$), but a close up of the activity near the sources. The colors represent the magnitude of this parameter. The red color corresponds to the highest value and the green/blue color the lowest value.

A possible explanation for the bending and merging effect can be found by looking at the Bernoulli equation:

$$\frac{1}{2}\rho u^2 + p + \rho g z = C \tag{4.1}$$

where $\rho\,[\text{kgm}^{-3}]$ is the density of the fluid, $u\,[\text{ms}^{-1}]$ the bulk speed of the fluid, $p\,[\text{Pa}]$ the pressure of the fluid, $g\,[\text{ms}^{-2}]$ the gravitational constant, $z\,[\text{m}]$ the vertical height of the fluid and $C\,[-]$ is a constant. In general, Bernoulli expresses a conversion between gravitation (i.e. buoyancy), kinetic energy (i.e. speed) and pressure.
The physical explanation for this 'bending' behaviour could be a kind of 'Bernoulli effect' (although formally the flow is not rotation-free as assumed in Bernoulli's law): due to energy conservation, higher velocities may coincide with lower local pressure, which may cause the updrafts to converge. However, we did not verify this hypothesis, such that this cannot be substantiated.

As seen before in section 4.1.1, the 'walls' of the domain have an effect on the outcomes of the simulation. In order to be able to neglect the effect of the 'walls' in this case study, the following value of $\Pi_2\,[-]$ is defined:

$$\Pi_2 = \frac{L_0 - d}{2 \cdot w} = 60 \tag{4.2}$$

This equation implies that when $d\,[\mathrm{m}]$ is adjusted ($w\,[\mathrm{m}]$ is constant), the domain size is also adjusted by the scaling above to make the effect of the 'walls' negligible. The results supporting equation 4.2 are in Appendix A.2.

Next, we investigate the quantitative effect of the distance between the sources, expressed in $\Pi_5 = d/w\,[-]$ with constant $w = 0.5\,\mathrm{m}$, on the total asymptotic kinetic energy $e^*_{asymp}\,[-]$. In figure 4.8 it can be seen that the distance does *not* have a clear effect on the kinetic energy. The maximum difference in the kinetic energy from the results is only 9% and no relation between $\Pi_5\,[-]$ and $e^*_{asymp}\,[-]$ can be found.

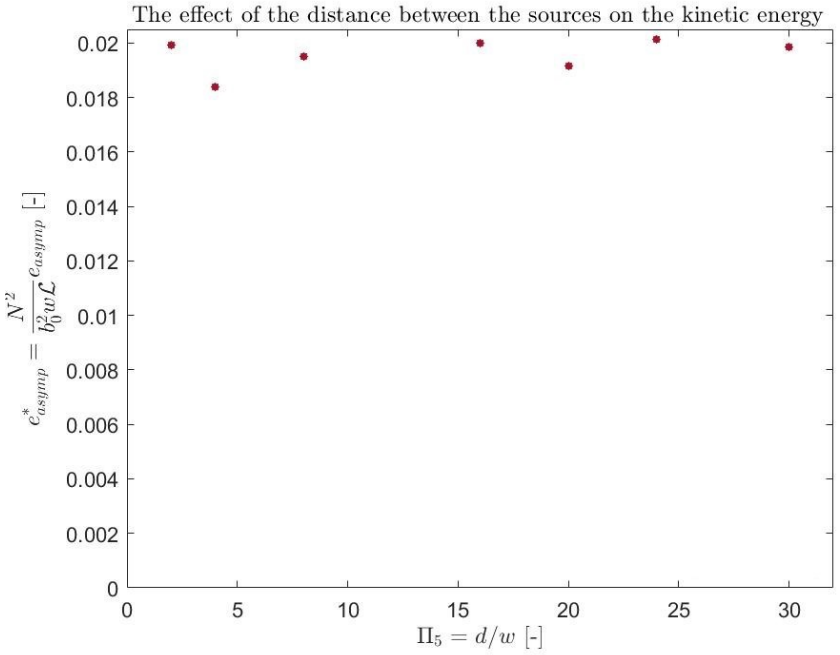

FIGURE 4.8: The effect of the distance between two sources $\Pi_5 = d/w\,[-]$ on the total asymptotic (steady state) kinetic energy $e^*_{asymp}\,[-]$ in the system.

To further check this result, the kinetic energy of different source configurations is studied. In table 4.1 the different cases and the asymptotic kinetic energy $e^*_{asymp}\,[-]$ are shown and in figure 4.9 the resulting kinetic energy $e^*\,[-]$ over time is shown. The kinetic energies in all the configurations are very alike and the maximum difference in the asymptotic kinetic energy $e^*_{asymp}\,[-]$ is only 5%. It can be concluded that the spatial distribution does *not* have an influence on the total kinetic energy in this 2D model. The deviant dissipative behavior in the 2D model makes it hard to say if this is also the case in real-life. Especially, since we will show that in the 3D simulation the behaviour will be rather different.

TABLE 4.1: Different cases with different configurations of the sources.

	# of sources	w_1[m]	w_2[m]	d[m]	b_0[ms^{-2}]	$e^*_{asymp}\cdot 10^3$ [-]
case a	1	1	-	-	1	18.3
case b	2	0.5	0.5	2	1	18.4
case c	2	0.4	0.6	2	1	18.4
case d	2	0.25	0.75	2	1	19.3

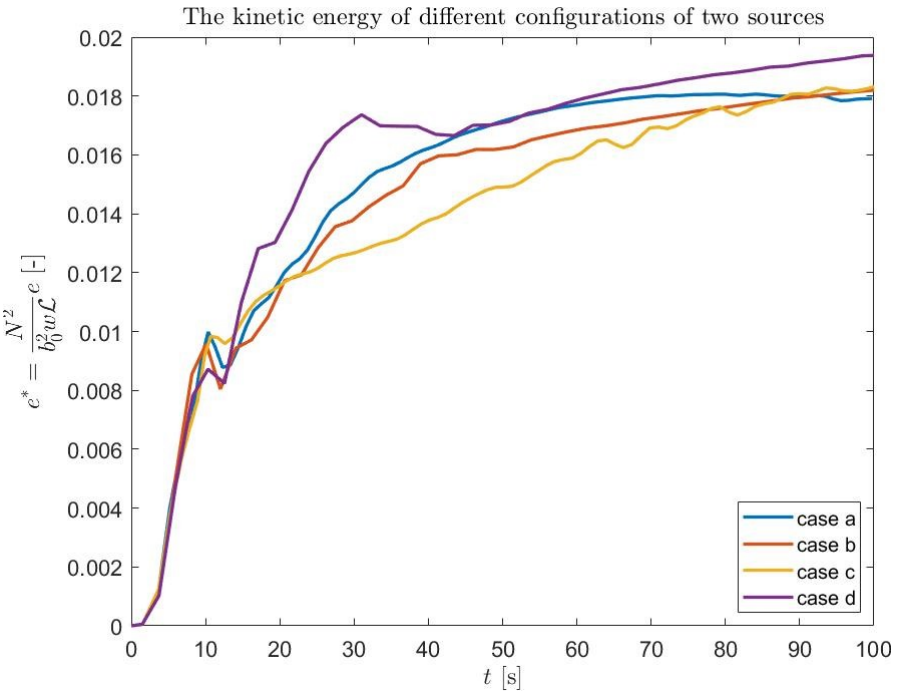

FIGURE 4.9: The kinetic energy e^* [−] over time of the 2D flow of four different source configurations, the cases are given in table 4.1.

4.1.3 Multiple heat sources (3D simulation)

The model is now extended to a three-dimensional setup. This means that the flow may generate 3D turbulence, such that i.e. vortex stretching is modelled. This mechanism makes the 3D model more reliable to give an indication about the real-life flow.

Two buoyancy sources of strength $b_0 = 1\,\mathrm{ms}^{-2}$, width $w = 0.5\,\mathrm{m}$, length $L_0 = 65\,\mathrm{m}$ and different distances $d\,[\mathrm{m}]$ between the sources are studied with the setup described in section 3.1.3.3. To make a physical interpretation of the results and visualize the flow, a 3D movie of the λ_2-isosurface [32] showing vortical structures is made, together with three 2D movies of a cross-section of the kinetic energy, the buoyancy and the gradient of the buoyancy. In figure 4.10 and 4.11 snapshots of the last time step of the movies

($t = 250\,\mathrm{s}$) are shown. The figures represent the 'steady state', which was reached after $t \approx 50\,\mathrm{s}$.

In figure 4.10 the sources are a distance $d = 2\,\mathrm{m}$ apart. From this figure, it is clear that the two plumes of the sources attract each other and bend towards the middle forming a single heat plume, as seen earlier in 2D. In figure 4.10b the kinetic energy of the two sources show a pattern similar to that of a single source (see figure 4.2). It seems like the distance between the sources is small enough to let the heat sources resemble and act like a single source.

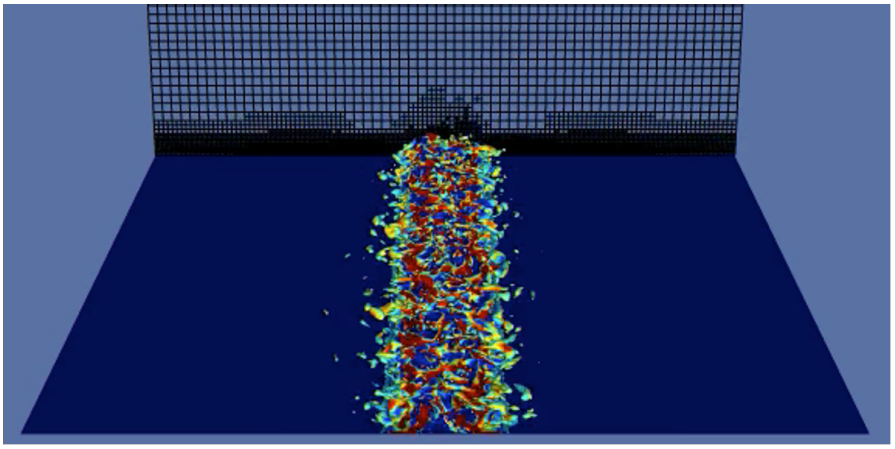

(A) The λ_2-isosurface [32], the color of the surface represent the upward velocity $u_y\,[\mathrm{ms}^{-1}]$. The back surface shows the number of grid cells.

(B) The kinetic energy.

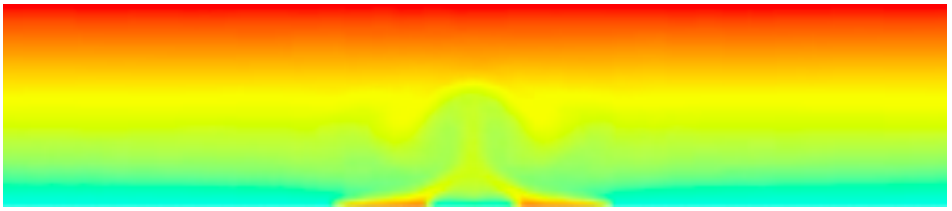

(C) The buoyancy.

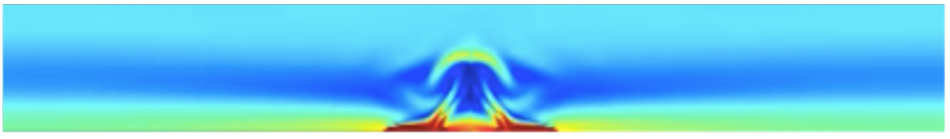

(D) The buoyancy field structure $\log(||\nabla b|| + 1)$

FIGURE 4.10: A spatial overview of four different parameters in the domain. Two sources with width $w = 0.5\,\mathrm{m}$ and strength $b_0 = 1\,\mathrm{ms}^{-2}$ a distance $d = 2\,\mathrm{m}$ apart in a domain $L_0 = 20\,\mathrm{m}$ are modelled in these figures. Figures 4.10b, 4.10c and 4.10d do not show the entire domain, but a close up of the activity near the sources and the figures are 2D cross-sections of the total domain. The colors represent the magnitude of this parameter. The red color corresponds to the highest value and the green/blue color the lowest value.

In figure 4.11 the sources are a distance $d = 4\,\text{m}$ apart. In figure 4.11 the sources do still attract each other (see figure 4.11c and 4.11d) but they do not merge, they really act like two individual sources. Concluding, the figures show a similar behaviour as in the 2D model: at close distances the sources merge and act like one single source and at further distances the sources do still attract but do not merge. This can again be explained by a conceptual interpretation of the Bernoulli equation (see equation 4.1). A clear difference with the 2D results is that the figures show more turbulent structures and eddies, which is also expected in reality.

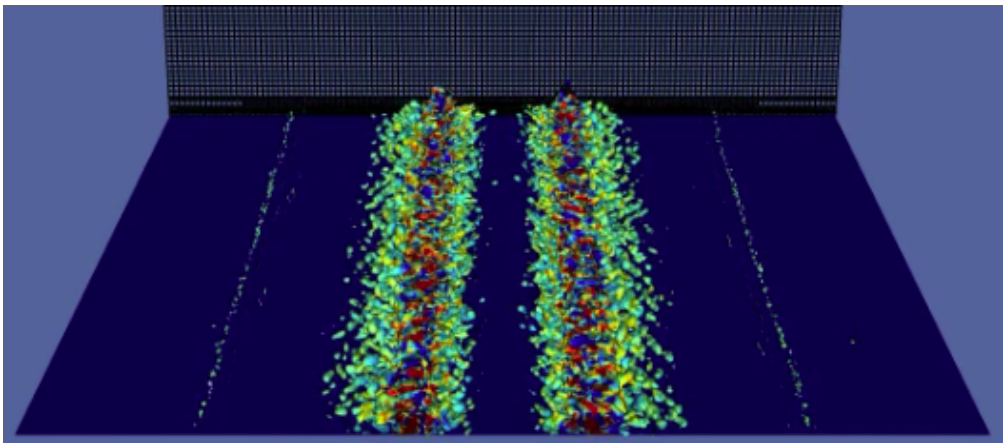

(A) The λ_2-isosurface [32], the color of the surface represent the upward velocity u_y. The back surface shows the number of grid cells.

(B) The kinetic energy.

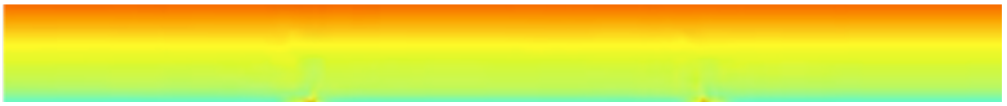

(C) The buoyancy.

(D) The buoyancy field structure $\log(||\nabla b|| + 1)$

FIGURE 4.11: A spatial overview of four different parameters in the domain. Two sources with width $w = 0.5\,\text{m}$ and strength $b_0 = 1\,\text{ms}^{-2}$ a distance $d = 4\,\text{m}$ apart in a domain $L_0 = 20\,\text{m}$ are modelled in these figures. Figures 4.11b, 4.11c and 4.11d do not show the entire domain, but a close up of the activity near the sources and the figures are 2D cross-sections at of the total domain. The colors represent the magnitude of this parameter. The red color corresponds to the highest value and the green/blue color the lowest value.

Again, the effect of the domain size is checked and the following value for Π_2 [−] is defined to neglect the effect of the 'walls':

$$\Pi_2 = \frac{L_0}{w} = 130 \tag{4.3}$$

This equation implies that L_0 [m] and w [m] are kept constant over the simulations. The results supporting this can be found in Appendix A.3.

To further study the behavior of the model, the effect of the viscosity on the kinetic energy in the system is also explored. This result can be found in Appendix A.4.

Lastly, the effect of the distance between the sources is checked again. The distance d [m], expressed in $\Pi_5 = d/w$ [−], between the sources is varied and the effect on the total asymptotic kinetic energy in the system e^*_{asymp} is studied. The results are shown in figure 4.12.

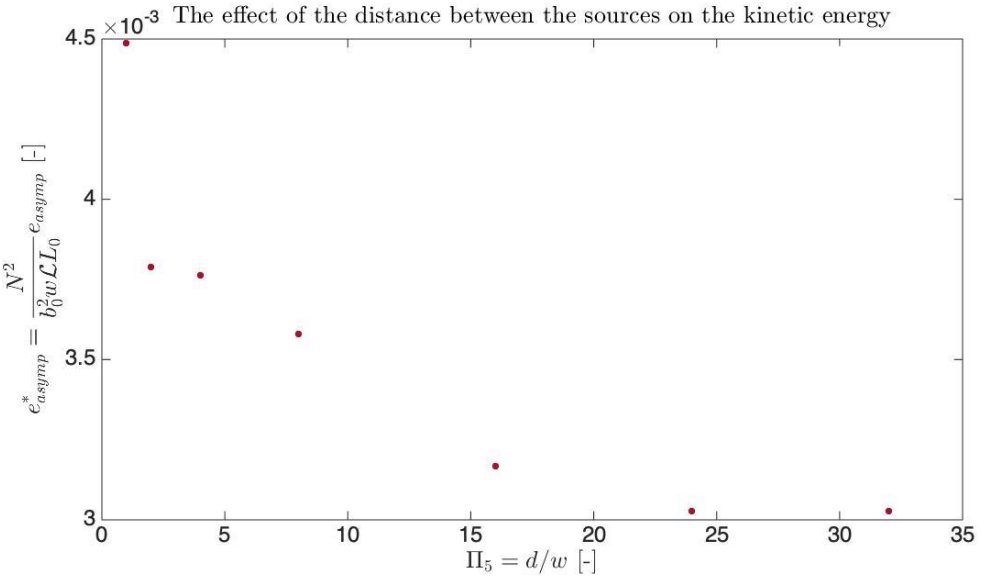

FIGURE 4.12: The effect of the distance between two sources expressed in $\Pi_5 = d/w$ [−] on the total asymptotic kinetic energy e^*_{asymp} [−] in the system.

The kinetic energy in the system shows a *decrease* with increasing distances between the sources until $\Pi_5 \approx 24$ [−], when the decrease appears to level off. This effect is also seen in the dissipation of the system (see figure A.10). It makes sense that those quantities show the same dependence, since all the kinetic energy will eventually dissipate in a system that is in equilibrium. This dependency indicates that the production of kinetic energy in the system is amplified if the sources are close together, as turbulent length scales increase. Also, the merging of the plumes above the sources possibly allows more effective rising of the energy. This can make the effect of the buoyancy source larger. This is a conceptual and rather qualitative explanation and needs further theoretical substantiation.

This result is rather different than the result obtained from the 2D simulation (see figure 4.8), where *no* dependence was found. This shows that not all results from 2D simulations can be extrapolated to a 3D situation, a check with a 3D model is needed.

4.1.4 The effect of surface-atmosphere coupling (2D simulation)

Here we briefly explore the coupling of the land-surface with the atmosphere in the 2D setup of section 3.1.3.4. The purpose of this section is merely to show that the simulations are feasible for future analysis. Due to time-constraints, no in-depth analysis could be made.

To compare the results to the previous case study without coupling (see section 4.1.2), movies of the buoyancy field and the gradient of the buoyancy field are made with the setup described in section 3.1.3.4. In figure 4.13 snapshots of the last time step of the movies ($t = 580\,\mathrm{s}$) are shown, they represent the 'steady state'. Also, in figure 4.14 the evolution of the kinetic energy $e\,[\mathrm{m^4 s^{-2}}]$, the dissipation of the kinetic energy $\epsilon\,[\mathrm{m^4 s^{-3}}]$ and the surface flux $-\Phi_{surface}\,[\mathrm{m^3 s^{-4}}]$ over time $t\,[\mathrm{s}]$ are shown.

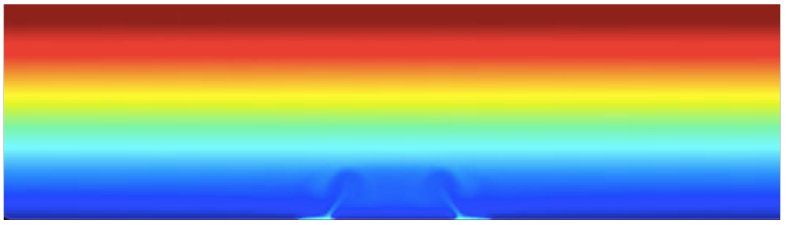

(A) Buoyancy.

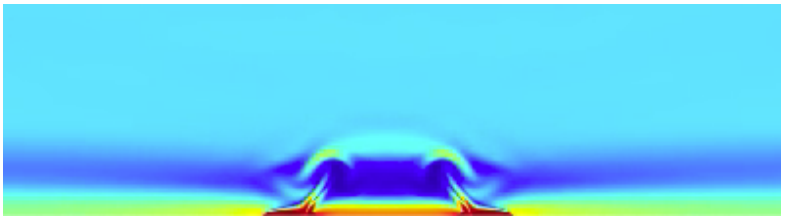

(B) Buoyancy gradient.

FIGURE 4.13: A spatial overview of two different parameters of two sources with width $w = 0.5\,\mathrm{m}$ a distance $d = 2\,\mathrm{m}$ apart. The buoyancy strength of the sources is a combination of the initial buoyancy $b_{(z=0)}\,[\mathrm{ms^{-2}}]$ and the lumped parameters $\Lambda_w, \Lambda_s\,[\mathrm{ms^{-1}}]$. The colors represent the magnitude of this parameter. The red color corresponds to the highest value and the green/blue color the lowest value.

The buoyancy field shows the same characteristics as the non-coupled buoyancy field (see figure 4.6): plumes are formed above the heat sources and they bend towards each other.

It can be seen that the kinetic energy and the kinetic energy dissipation fluctuate more over time (see figure 4.14) as compared to earlier non-coupled results in figure 4.2. The surface flux is not constant over time in this model, it starts high and decreases over time. This makes sense, since the surface heterogeneity initially begins with a buoyancy

value of $b_0\,[\mathrm{ms}^{-2}]$ and is cooled over time by a negative $R^*\,[\mathrm{m}^2\mathrm{s}^{-3}]$ and subsequently the surface flux will decrease.

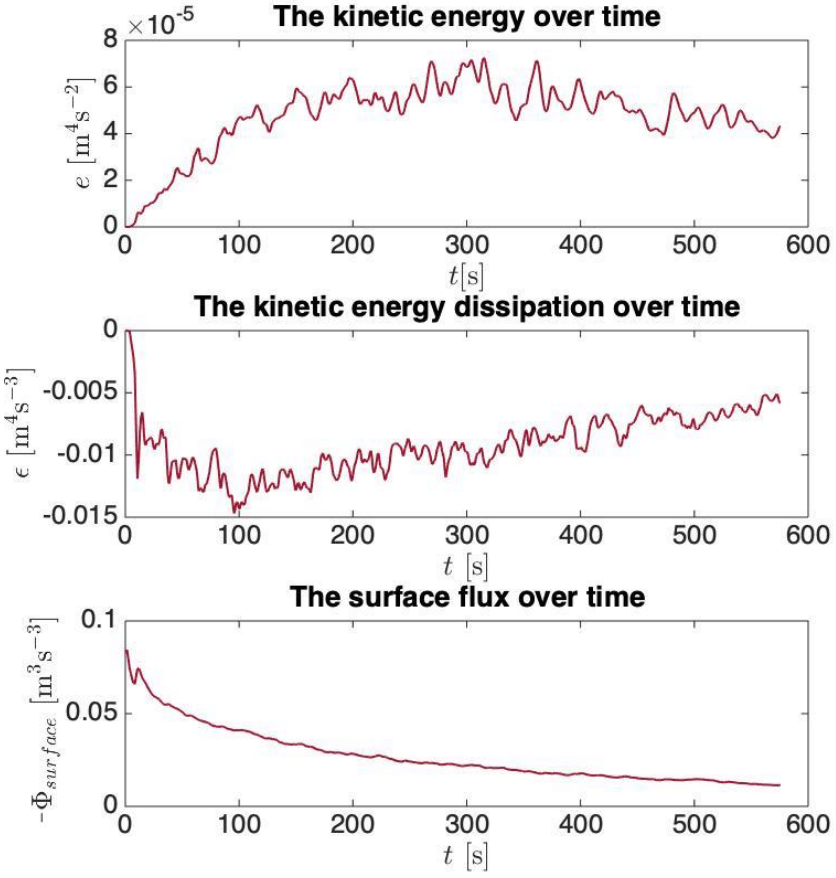

FIGURE 4.14: The evolution of the total kinetic energy $e\,[\mathrm{m}^4\mathrm{s}^{-2}]$, kinetic energy dissipation $\epsilon\,[\mathrm{m}^4\mathrm{s}^{-3}]$ and surface flux of the source $-\Phi_{surface}\,[\mathrm{m}^3\mathrm{s}^{-3}]$ over time $t\,[\mathrm{s}]$.

4.2 Results of the field experiment

In this section the results of the field experiment to capture the temperature flow above surface heterogeneity with the setup explained in section 4.2 are presented.
The snapshots of the screen presented in this section have been smoothed by an averaging filter to reduce the noise. The original snapshots are shown in Appendix B.1. The filter is justified since the original images show noise in the form of clear contrast in neighboring pixels, such a contrast is not present in reality. The filter replaces every pixel with the average of the 3×3 pixels surrounding the pixel.

4.2.1 Experiment above natural surface heterogeneity

An example of a typical snapshot of the 'air temperature', so the screen temperature corrected by the emissivity (see equation 3.34) and with an averaging filter applied, is shown in figure 4.15. The upper part of the figure clearly shows higher temperatures than the lower part of the figure, which indeed indicates that the lower atmosphere is stably stratified. The effect of the surface heterogeneity (a road plate on bare soil) can not clearly be seen in this snapshot. Further analysis of all snapshots also does not show a discernable effect. The surface temperature of the road plate has not been measured. Therefore it is not known if the road plate has effectively stored heat during the day, causing it to turn into a heat source during the night. It is likely that the road plate is heated during the day, but that the bare soil underneath is actually isolated by the plate and the air layer. The road plate is only a couple of centimeters thick, so this plate is also easily cooled by loss of radiation during the night. From experience it is e.g. known that thin (metal) bridges are very susceptible to road frost, due to the fact that they are isolated surfaces, without contact to the ground (personal communication Van de Wiel). Since the measurements are not performed immediately after sunset (sunset at 21:26:00, measurements started at 23:37:00), this may be an explanation for not seeing any buoyancy effects above the road plate. In future research it is recommended to also measure the surface temperature.

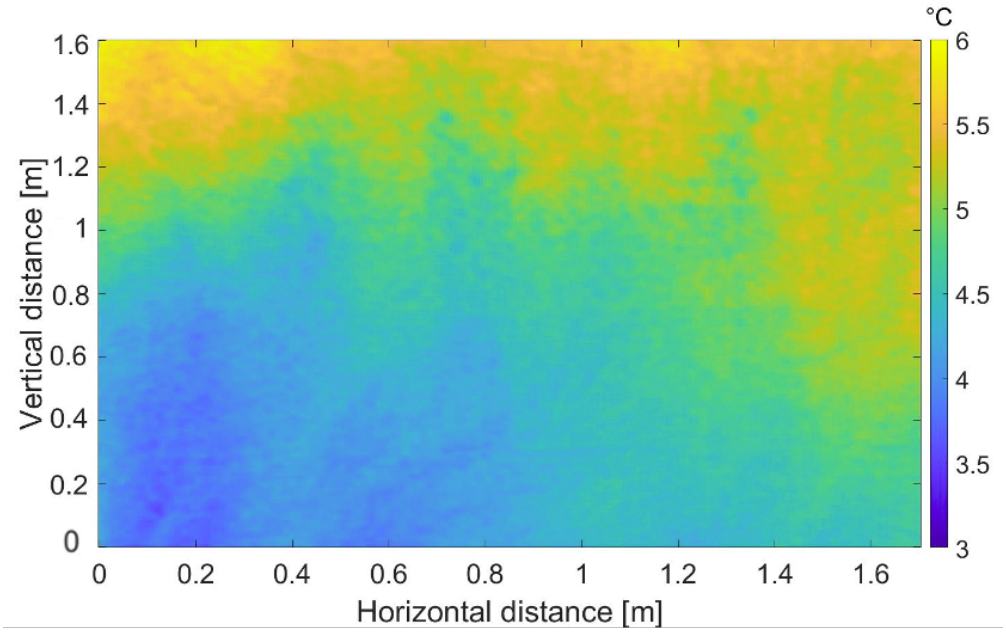

FIGURE 4.15: A snapshot of the 'air temperature', measured by the screen, at 23:41:30 on April 13th in Krabbendijke. The unfiltered figure is presented in Appendix B.1

The results can not be used to study the effect of a natural surface heterogeneity, but by further analysis the stability of the atmosphere during this night can be quantified. This can be useful background knowledge for the results of the experiment above the artificial heat sources.

The temperature of this snapshot is averaged over the full horizontal domain to give an average temperature-height profile (blue line in figure 4.16). The temperature does vary in the horizontal direction, to show this variation the standard deviation is also shown (gray shade). Lastly, a linear least square fit (red line) is applied to calculate the inversion strength in the form of the lapse rate Γ [Km^{-1}].

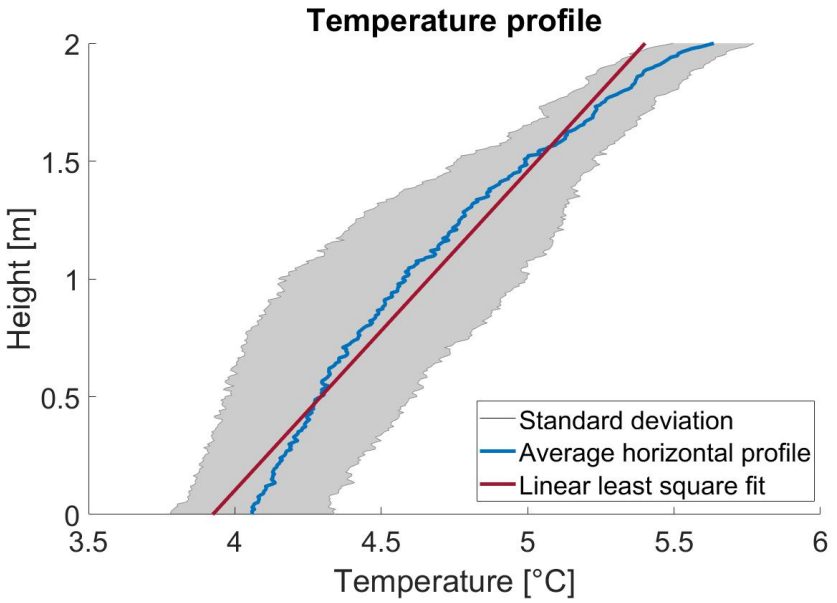

FIGURE 4.16: The temperature-height profile at 23:41:30. The gray shade shows the standard deviation of the temperatures measured at a height, the blue line shows the average temperature at one height and the red line shows the linear least square fit of the temperature profile. The linear least square fit is given by: $T = 0.7 \cdot h - 3.9$, where $T\,[°\mathrm{C}]$ is the temperature, $h\,[\mathrm{m}]$ is the height and the lapse rate $\Gamma = 0.7\,\mathrm{Km}^{-1}$.

Clearly, the profile in figure 4.16 is non-linear. However, it is interesting to quantify the stratification strength during measurements. Therefore the profile is characterised by a linear least square fit (like in figure 4.16) as a proxy. The linear least square fit $T = \Gamma \cdot h + T_0$ is calculated for all snapshots over time, where $T\,[°\mathrm{C}]$ is the temperature, $\Gamma\,[\mathrm{Km}^{-1}]$ is the linear lapse rate, $h\,[\mathrm{m}]$ is the height and $T_0\,[°\mathrm{C}]$ the temperature at $h = 0\,\mathrm{m}$. These results are shown in figure 4.17. The gray shaded errorbars are the uncertainties of the linear least square fits.

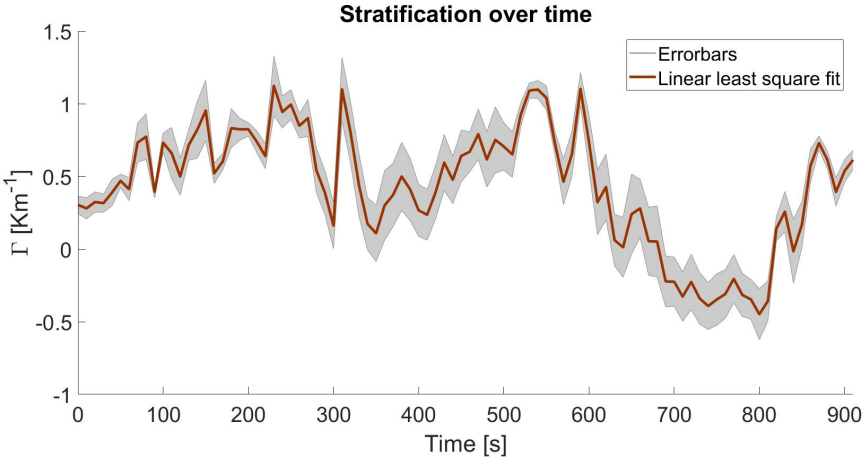

FIGURE 4.17: The linear lapse rate $\Gamma\,[\mathrm{Km}^{-1}]$ over time, the gray shaded errorbars show the error of the least square fits.

It can be seen that the lapse rate does vary over time, but is mainly positive corresponding to a stably stratified atmosphere. Interestingly, the lapse rate at some point becomes negative. Most likely this is caused by an advective event or turbulent gust, where warm air is blow over the surface.

4.2.2 Experiment above artificial surface heterogeneity

Some additional difficulties came up during the measurements of this experiment, causing the circumstances not the be as initially preferred (stable conditions). The experimental site was on a pear orchard in Krabbendijke (Zeeland, The Netherlands, 51°25'44.7"N, 4°48'8.5"E). There are wind machines installed in the orchard to prevent fruit frost damage on the pears. The wind machines will automatically start working when the temperature drops below 2 °C. Due to air mixing with air above, local (near) surface temperatures will raise than. Our experiment was performed with the wind machines active and thus having an influence on the local temperature and wind. The effect is discussed in the "Intermezzo" of this section. Additionally, some clouds appeared, which causes the stratification to weaken. Interestingly, both effects cause the lapse rate to reverse at occasions. This is also showed by the lapse rate over time in figure 4.18 (calculated as explained in section 4.2.1).

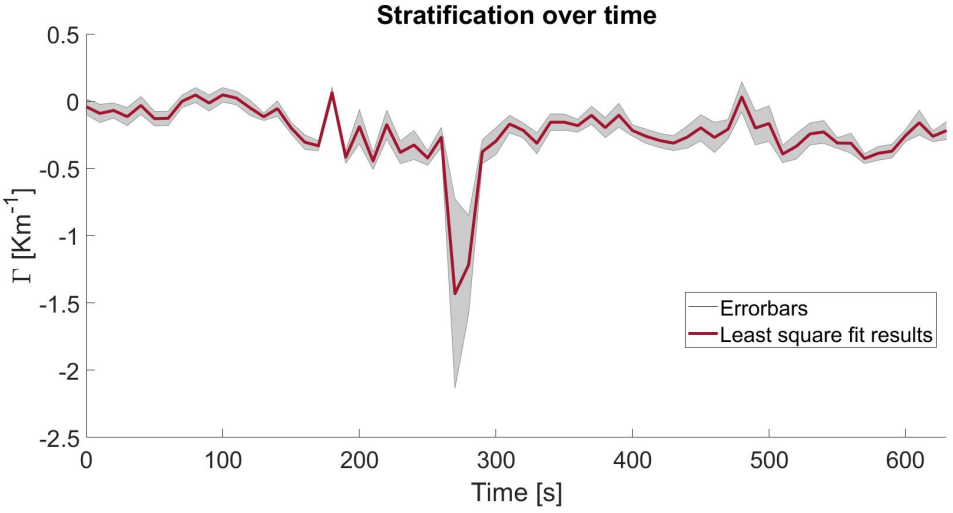

FIGURE 4.18: The linear lapse rate $\Gamma\,[\mathrm{Km}^{-1}]$ over time calculated by linear least square fits over time (started at 00:46:04 on April 14th), the gray shaded errorbars show the error of the least square fits. The dip around $t = 280\,\mathrm{s}$ is caused by a person walking in front of the screen to displace the sources and can thus be neglected.

To study the results of the effect of the heat sources, a snapshot with a positive lapse rate is selected for the boxes close together ($d = 0.5\,\mathrm{m}$) and far apart ($d = 1.2\,\mathrm{m}$). The selected moments are at $t = 90\,\mathrm{s}$ with $\Gamma = 0.05\,\mathrm{Km}^{-1}$ and at $t = 490\,\mathrm{s}$ with $\Gamma = 0.03\,\mathrm{Km}^{-1}$ respectively. The 'air temperature' of the selected snapshots are shown in figure 4.19 and 4.20.

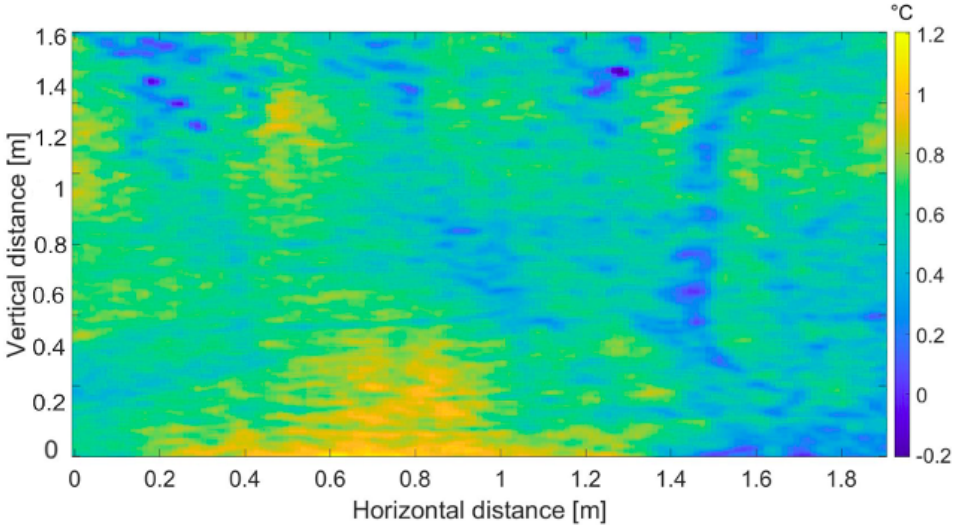

FIGURE 4.19: A snapshot of the 'air temperature' with two artificial heat sources (horizontal distance: $0.4 - 0.6\,\text{m}, 0.85 - 1.1\,\text{m}$) under the screen at 00:51:04 on April 14th in Krabbendijke. The unfiltered figure is presented in Appendix B.1.

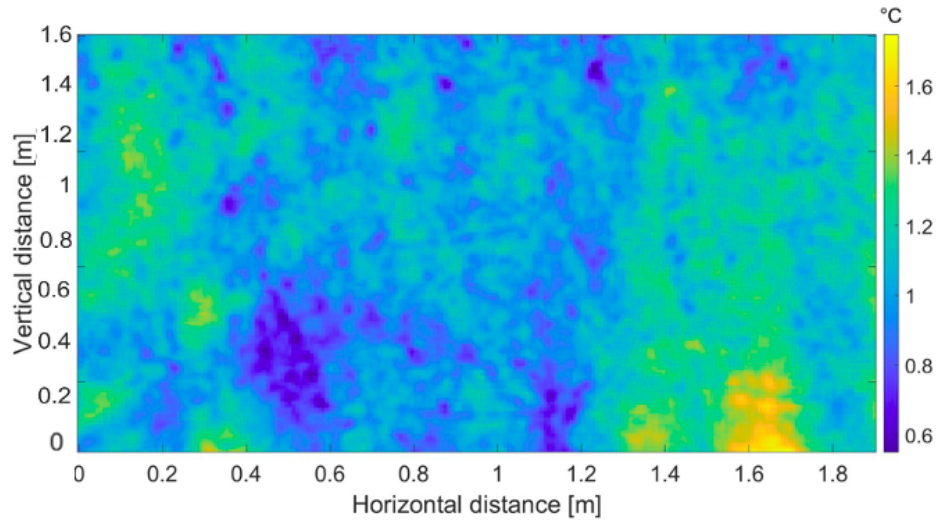

FIGURE 4.20: A snapshot of the 'air temperature' with two artificial heat sources (horizontal distance: $0.3 - 0.5\,\text{m}, 1.5 - 1.75\,\text{m}$) under the screen at 00:57:44 on April 14th in Krabbendijke. The unfiltered figure is presented in Appendix B.1.

A couple of similarities between the snapshots and the results of the simulations can be identified. The influence of the heat sources shows a heated plume above the source with a finite length, this can be best seen in figure 4.20 above the right source. If the sources are close together the heat plumes seem to merge and form one heat plume (see figure 4.19). If the sources are further apart two separate plumes are visible (see figure 4.20), the attraction between the plumes is not seen in this case. The nuance must be made that the plumes are not clearly visible in all individual snapshots over time. Probably because of clouds and wind gusts, and the conclusions above are thus not strongly justified.

Intermezzo: Effect of the wind machine

The effect of the wind machine on the local temperature is not relevant for answering the main question of this report, but it is an interesting side result. It shows the potential for using the setup with the screen (section 3.2) to quantify near-surface air temperature variations.

The wind machine that was active during these measurements rotated at 540 rpm and the fan hub revolved around the tower with a period $T_{hub} = 300\,\text{s}$. The screen is placed at a distance $d = 95 \pm 5\,\text{m}$ in the NNW-direction of the machine. The wind machine ensures mixing of the colder air close to the surface with the warmer air from above, causing the local temperatures to raise near the surface. A previous study [33] at the same location used DTS cables to determine the effect of the wind machine on the local temperature at different heights and different distances from the fan in the pear trees of the orchard. In this study the screen was placed on an open part of the field measuring the air temperature (see figure 3.10), the rest of the setup is comparable to the previous setup [33].

FIGURE 4.21: The wind machine in field. Figure adapted from [33].

In figure 4.22 the average temperature over time is shown, the errorbars are the standard deviations of the average temperature. There is a clear temperature variation over time visible, the two peaks in temperature correspond to the moments the fan hub was directed towards the screen. The two temperature peaks show an amplitude variation of $T_{ampl} = 3.2 \pm 0.6\,\text{K}$. The time between the peaks is $T_{peaks} = 310 \pm 10\,\text{s}$, which is in correspondence with the rotation period of the hub T_{hub}. Also, the variation of temperature over time shows strong resemblance with the result from the previous study [33].

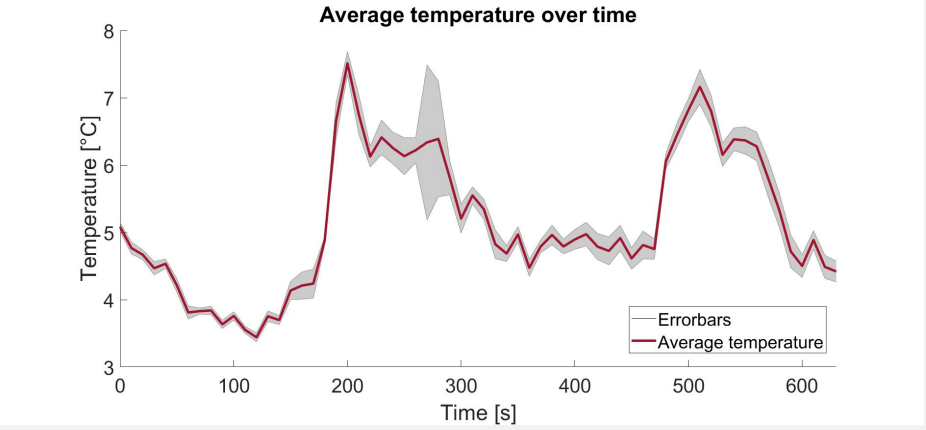

FIGURE 4.22: The 'air temperature' averaged for the screen over time. Two clear peaks can be identified that correspond to the rotation of the ventilator. The peak in standard deviation around $t = 280\,\text{s}$ is caused by a person walking in front of the screen to displace the heat sources.

The temperature at different heights is also studied over time. This gives insight in the effect of the wind turbine on the temperature at different heights and the stability of the atmosphere. It can be seen that the atmosphere is no longer stably stratified because of the mixing and the wind machine has a similar effect at all heights.

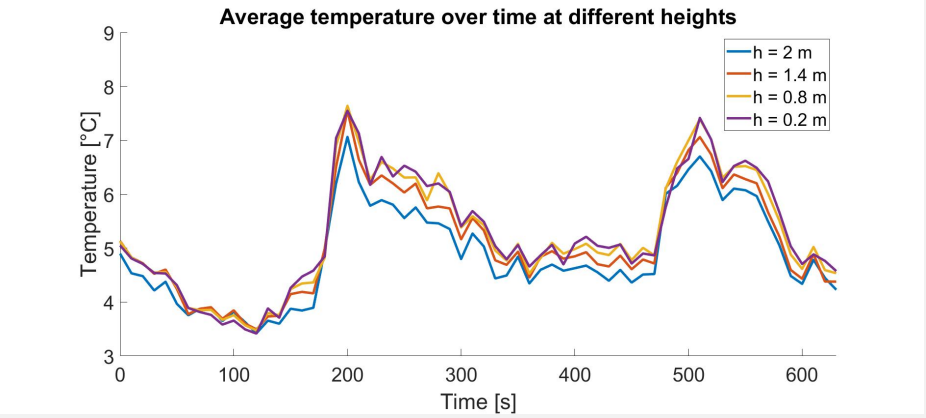

FIGURE 4.23: The 'air temperature' averaged over the horizontal domain of the screen at height h [m] over time.

Chapter 5

Conclusion

This study aims to look into the effect of small-scale surface heterogeneity on the mixing in the stable atmosphere and the effect of the spatial distribution of different surface heterogeneities. The understanding of the stable boundary layer (SBL) and its representation in numerical weather predictions (NWP) is still a challenge. The effect and representation of surface heterogeneity is part of this challenge. It is likely that spatially distributed surface heterogeneities (e.g. a ditch or a road) turn into buoyancy sources during the night, because they are thermal memories of the daytime heating. These buoyancy sources can cause turbulent mixing. Therefore, it would be highly desirable to better understand the effect of surface heterogeneity. To do so, simulations and field experiments are carried out to answer the research questions:

What is the effect of small-scale surface heterogeneity on the mixing properties within the stable boundary layer? What impact do different configurations of the heterogeneity have on this mixing?

A simulation is setup and several case studies are performed. The simulation focuses on the effect of heaviside buoyancy sources on a SBL and the effect of the distance between two heaviside buoyancy sources on the total kinetic energy in the system. The main conclusions of the case studies are:

- *One heat source (2D simulation)*
  A heat plume with finite length is formed above the surface buoyancy source. This was also expected from physical interpretation of a positive buoyancy surface force in a stably stratified boundary layer.

- *Multiple heat sources (2D simulation)*
  The heat plumes are attracted towards each other. At small distances they even merge and act like a single heat source. This can be explained by an interpretation of the Bernoulli equation (see equation 4.1), but more theoretical foundation is

needed to explain this phenomenon. The distance between the sources and their spatial distribution do not show a clear influence on the total kinetic energy in the system.

- *Multiple heat sources (3D simulation)*
  The attraction between the buoyancy plumes and the merging at small distances is also observed in this 3D model. Unlike in the 2D model, a clear effect of the distance between the sources on the kinetic energy is observed. At smaller distances (distance $d < 12\,\mathrm{m}$ for sources with width $w = 0.5\,\mathrm{m}$), an increase in distance yields a decrease in kinetic energy in the system. At larger distances (distance $d > 12\,\mathrm{m}$ for sources with width $w = 0.5\,\mathrm{m}$) this effect disappears. Apparently, the bending and merging of the plumes allows turbulent length scales to increase leading to more release of buoyancy and hence higher turbulent kinetic energy. This observed phenomena lacks further theoretical foundation.

- *The effect of surface-atmosphere coupling (2D simulation)*
  This model can be used as inspiration for future research. The model shows results comparable to the model without surface-atmosphere feedback. Two attracting buoyancy plumes are formed above the sources. The surface-atmosphere coupling causes the surface flux to decrease over time due to a surface cooling feedback driven by long-wave radiation and ground heat transport.

Comparing the case studies, the 2D simulation shows a different conclusion than the 3D model. Since the 3D model is able to describe real-life turbulent flows and dissipation more accurate, it is likely that these results come closest to reality. It is therefore recommended to use the 3D model in future studies.

To check if the results of the simulations are in correspondence with the real-life effect of surface heterogeneity, two field experiments are performed. The main conclusions of the two field experiments are:

- *Experiment above natural surface heterogeneity*
  The used natural surface heterogeneity (a road plate on bare soil) does not show a clear influence on the thermal stratification. It is likely that the assumption of the road plate on bare soil acting as heat source during the night was incorrect. Unfortunately, no conclusions about the effect of a natural surface heterogeneity on the SBL can be drawn.

- *Experiment above artificial surface heterogeneity*
  A heat plume with finite length can be seen above the artificial heat sources (two warm water baths). If the heat sources are close together ($d = 0.5\,\mathrm{m}$) the plumes seem to merge and at larger distances ($d = 1.2\,\mathrm{m}$) they form separated plumes. This same effect is observed in the simulations and this experiment therefore endorses the result of the simulations. The nuance must be made that the plumes are not

clearly visible in all snapshots over time and the conclusion is thus not strongly substantiated.

Overall it can be concluded that this experimental setup can be used to look into temperature flows above surface heterogeneity in future research. Finally, as a side-result it was found that the screen set-up was very useful in quantifying near surface 'heat events' caused by the rotation of a wind machine present at the experimental field site.

5.1 Recommendations

The first steps have been taken to characterize the effect of surface heterogeneity on the SBL and eventually develop a parametrisation for sub-grid surface heterogeneity in NWP models. Still a lot of follow-up research is needed to achieve this final goal. Recommendations for follow-up research are:

- The simulation model can be extended and improved on many points. The surface-atmosphere feedback model can be used as starting point. Additional sensitivity studies for the parameters of the model have to be performed and more observational substantiation for the parameters is also needed. Finally, the outcomes also have to be verified with observations to justify the simplifications (e.g. ignorance of moisture) of the model.
- Theoretical analysis of the governing equations and analysis of e.g. TKE budget equations could further clarify on the actual physical mechanism behind the bending and merging of the plumes and the effect of the distance between heat sources on the total kinetic energy.
- The experimental setup of the screen can be used for follow-up experiments. It would be interesting to place the screen above a ditch (hypothetical heat source) on a stable night. It would be recommended to measure the screen temperature during an entire night, because the effect can be variable during the night. Also, additional measurements of the surface temperature of the water are necessary to complement the measurements of the air temperature.
- It would be interesting to set up an experiment to look at the effect of surface heterogeneity on a larger scale. Setting up an experiment with DTS cables on a site with surface heterogeneities of several scales will give a lot of insights. Measuring a horizontal and vertical profile of air temperature with DTS cables combined with measurements of the surface temperature of the area (by sensors or infrared camera's) will give more insight in the scales of real-life surface heterogeneity and will be relevant towards a parametrization of its effect.

Appendix A

Simulation: Additional results

A.1 Example of a convergence study

In the simulation models an adaptive grid is used as described in section 3.1.1. The parameters that determine the adaptive grid must not have an influence on the outcomes, since they are non-physical parameters. To ensure this, the influence of these parameters at every domain size L_0 [m] is studied in a convergence study. In the convergence study the accuracy of the results needs to be weighted against the execution time. The values that are presented in section 4.1 are the optimal results that came out of the convergence study. A detailed example of the convergence study of the 2D model with a single buoyancy source (for the setup see section 3.1.3.1) in domain $L_0 = 10\,\text{m}$ is shown in the following tables and figures. This method for the convergence study is applied to produce all the results presented in section 4.1.

Looking at figure A.2, it can be concluded that "case d" of table A.1 is the best case to use for the maximum and minimum refinement level. The difference in the kinetic energy is 2.93% between "case a" en "case d", while the execution time $t_{execution}$ [s] is reduced with 89.5%. So the maximum and minimum refinement level at $L_0 = 10\,\text{m}$ should be 9 and 6 respectively.

TABLE A.1: The different cases to study the convergence of the model for the maximum and minimum refinement level for the setup of section 3.1.3.1 with $L_0 = 10\,\mathrm{m}$ and a source with strength $b_0 = 2\,\mathrm{ms}^{-2}$ and width $w = 1\,\mathrm{m}$.

	max	min	$e^*_{asymp} \cdot 10^3$ [-]	$t_{execution}$ [s]
case a	9	6	3.06	294.8
case b	9	5	2.88	150.6
case c	8	5	2.97	47.44
case d	8	4	2.97	30.91
case e	7	4	1.81	7.056
case f	8	3	$1.422 \cdot 10^{-6}$	0.3544

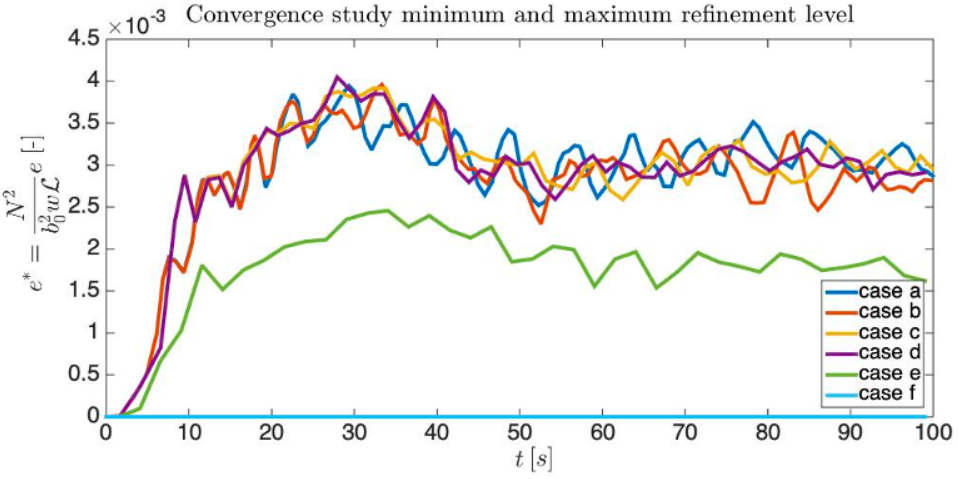

FIGURE A.1: The evolution of the dimensionless kinetic energy over time for the different cases of the convergence study shown in table A.1

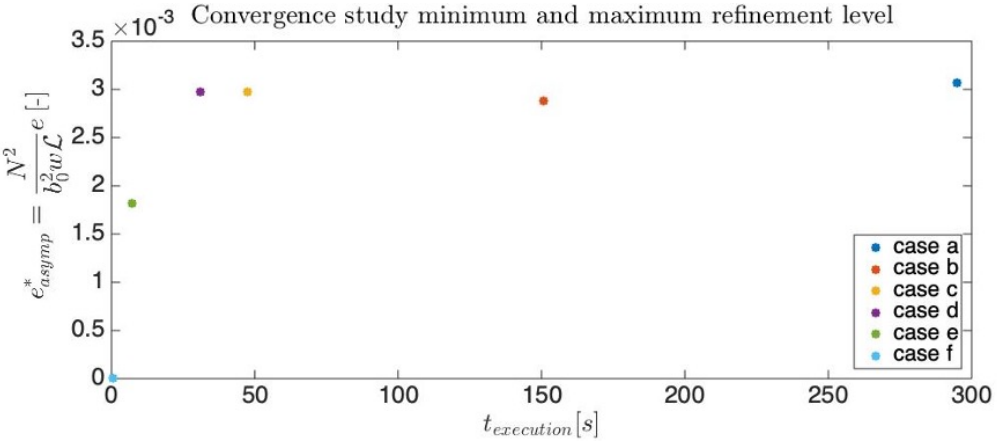

FIGURE A.2: The asymptotic values of the dimensionless kinetic energy versus the execution time of the model for the different cases of the convergence study shown in table A.1.

Looking at u_x [ms^{-1}] in figure A.3, it can be concluded that the asymptotic kinetic energy does not vary significantly over the different cases. The difference between the highest ("case a") and lowest ("case e") value is only 6.02%. Since "case b" is the most accurate case and the asymptotic kinetic energy of "case e" only differs 0.86% from "case b" and the execution time $t_{execution}$ [s] is reduced with 51.5%, "case e" has the best value for u_x [ms^{-1}] to use.

Looking at u_y [ms^{-1}] in figure A.3, it can be concluded that the asymptotic kinetic energy does not vary significantly over the different cases. The difference between the highest ("case a") and lowest ("case e") value is only 5.89%. Since "case b" is the most accurate case and the asymptotic kinetic energy of "case f" only differs 0.46% from "case b" and the execution time $t_{execution}$ [s] is reduced with 8.18%, "case f" has the best value for u_y [ms^{-1}] to use.
Concluding, for $L_0 = 10\,\text{m}$ the values $u_x = 0.5\,\text{ms}^{-1}$ and $u_y = 1\,\text{ms}^{-1}$ are chosen.

TABLE A.2: The different cases to study the convergence of the model for the refinement condition for the velocities in the x- and y-direction u_x, u_y [ms^{-1}] for the setup of section 3.1.3.1 with $L_0 = 10\,\text{m}$ and a source with strength $b_0 = 2\,\text{ms}^{-2}$ and width $w = 1\,\text{m}$.

		u_x [ms^{-1}]	u_y [ms^{-1}]	$e^*_{asymp} \cdot 10^3$ [-]	$t_{execution}$ [s]
u_x	case a	0.01	0.01	2.97	30.91
	case b	0.005	0.01	2.82	34.36
	case c	0.05	0.01	2.81	18.63
	case d	0.1	0.01	2.82	16.82
	case e	0.5	0.01	2.79	16.65
	case f	1	0.01	2.79	19.30
u_y	case a	0.01	0.01	2.97	30.91
	case b	0.01	0.005	2.81	26.03
	case c	0.01	0.05	2.92	24.23
	case d	0.01	0.1	2.84	25.15
	case e	0.01	0.5	2.80	24.17
	case f	0.01	1	2.80	23.90

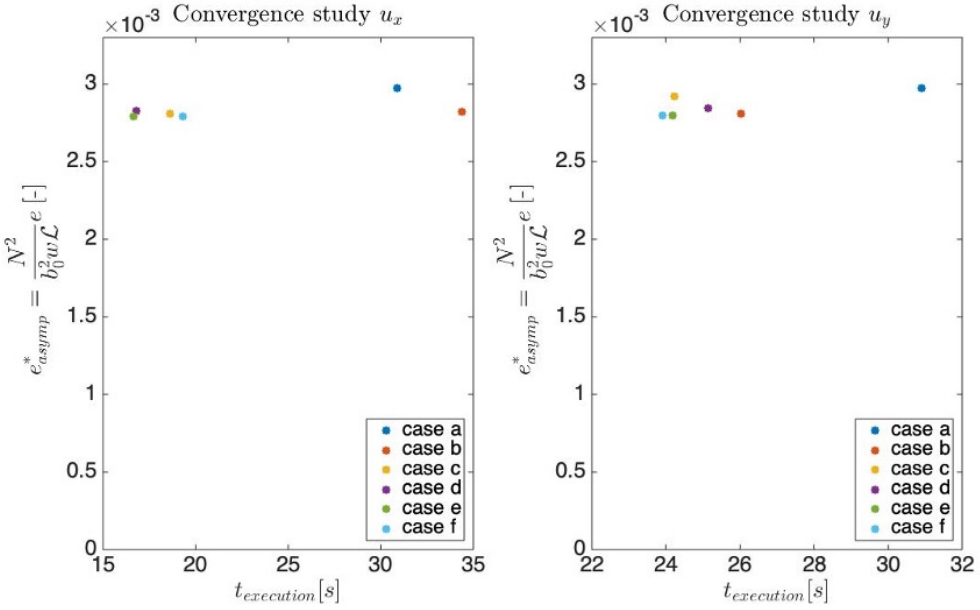

FIGURE A.3: The asymptotic values of the dimensionless kinetic energy versus the execution time of the model for the different cases of the convergence study shown in table A.2.

Looking at figure A.4, it can be concluded that the asymptotic kinetic energy does not vary significantly over the different cases. The difference between the highest ("case a") and lowest ("case c") value is only 8.61%. Since "case a" is the most accurate case and the asymptotic kinetic energy of "case f" only differs 0.83% from "case a" and the execution time $t_{execution}$ [s] is reduced with 45.6%, "case f" has the best value for $b\,[\mathrm{ms}^{-2}]$ to use. So the refinement condition for $b\,[\mathrm{ms}^{-2}]$ at $L_0 = 10\,\mathrm{m}$ is set to $b = 1\,\mathrm{ms}^{-2}$.

TABLE A.3: The different cases to study the convergence of the model for the refinement condition for the buoyancy $b\,[\mathrm{ms}^{-2}]$ for the setup of section 3.1.3.1 with $L_0 = 10\,\mathrm{m}$ and a source with strength $b_0 = 2\,\mathrm{ms}^{-2}$ and width $w = 1\,\mathrm{m}$.

	$b\,[\mathrm{ms}^{-2}]$	$e^*_{asymp} \cdot 10^3$ [-]	$t_{execution}$ [s]
case a	0.01	3.07	28.68
case b	0.02	2.92	22.11
case c	0.04	2.81	18.63
case d	0.2	3.01	15.88
case e	0.4	2.99	16.74
case f	1	3.05	15.59

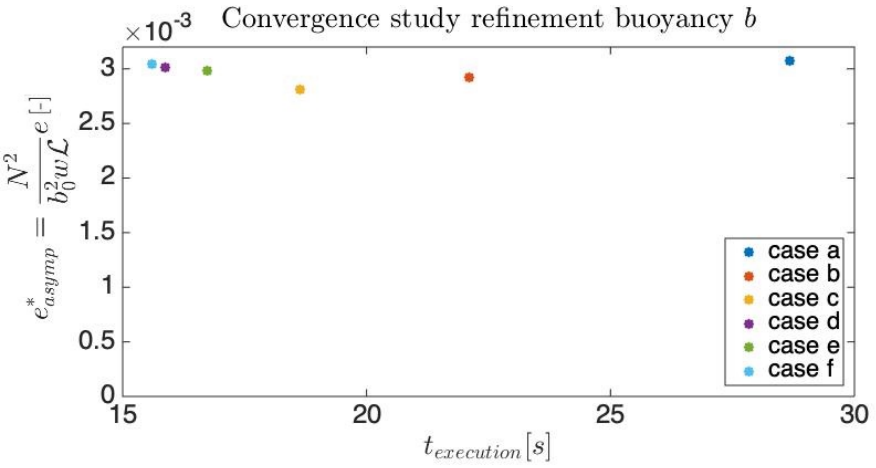

FIGURE A.4: The asymptotic values of the dimensionless kinetic energy versus the execution time of the model for the different cases of the convergence study shown in table A.3.

A.2 Multiple heat sources (2D simulation): Effect of the domain size

The 2D model with one heat source pointed out the effect of the 'walls' on the system (see section 4.1.1). This effect also needs to be eliminated for the results with two heat sources (section 4.1.2), since there are no 'walls' in reality. The hypothetical condition to eliminate this effect with two heat sources is derived from the results of the case study with one heat source (see section 4.1.1):

$$\Pi_2 = \frac{L_0 - d}{2 \cdot w} \tag{A.1}$$

In figure A.5 this condition is checked for the setup of section 3.1.3.2 with two sources ($d = 1\,\text{m}$ and $w = 0.5\,\text{m}$). The difference in the dimensionless asymptotic kinetic energy in the range $L_0 = 50 - 70\,\text{m}$ is 7.06% and in this range the kinetic energy $e^*_{asymp}\,[-]$ does not unambiguously increase with $\Pi_2\,[-]$. This verifies the condition in equation A.1. This definition of $\Pi_2\,[-]$ is chosen in the setup of section 3.1.3.2.

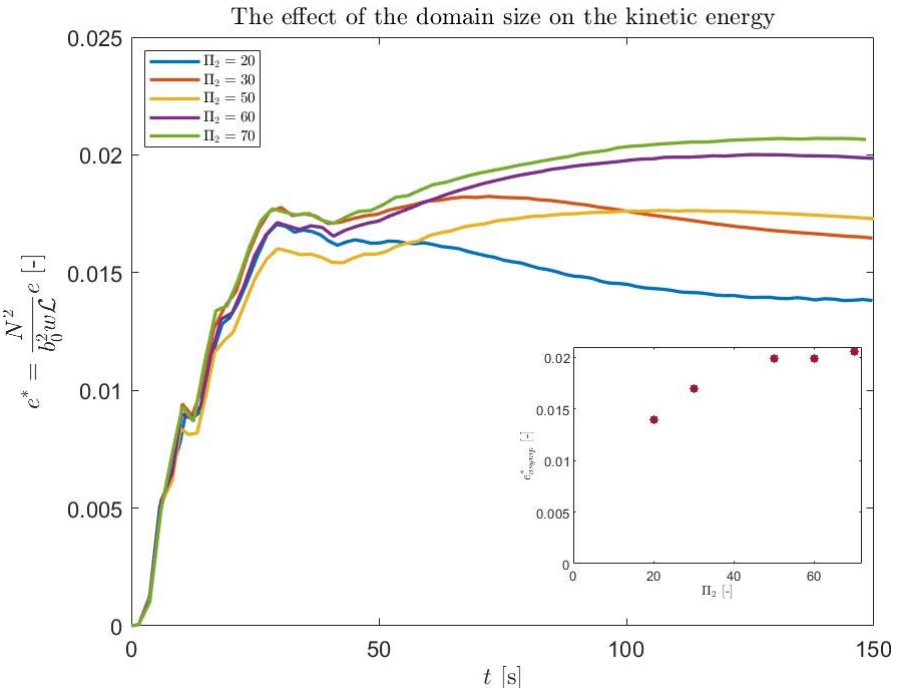

FIGURE A.5: The kinetic energy e^* [−] over time t [s] for different domain sizes L_0 [m] and thus different values of Π_2 [−] (d [m] and w [m] constant). In the figure in the right corner the relation between the asymptotic kinetic energy e^*_{asymp} [−] and Π_2 [−] is shown.

A.3 Multiple heat sources (3D simulation): Effect of the domain size

For the 3D model with two heat sources (see section 3.1.3.3) the effect of the domain size L_0 [m] is checked again to find the condition to eliminate the effect of the 'walls'. The effect is shown in figure A.6. For $\Pi_2 < 30$ [−] the asymptotic kinetic energy e^*_{asymp} [−] increases with increasing Π_2 [−]. For $\Pi_2 > 30$ [−] the asymptotic kinetic energy e^*_{asymp} [−] starts decreasing with increasing Π_2 [−]. This result can be explained by the movies of the vortical structures. For $\Pi_2 < 30$ [−] the movies show a clear damping of the vortices at the left and right boundary, causing the vortices to be driven upward (see figure A.7). For $\Pi_2 > 30$ [−] the vortices do not seem to be affected by the 'walls' (see figure 4.10 and 4.11). The decrease in asymptotic kinetic energy e^*_{asymp} [−] (for $\Pi_2 > 30$ [−]) is probably caused by the scaling of the length of the buoyancy sources with the domain size L_0 [m]. The dimensionless kinetic energy (see equation 3.23) is scaled linearly with this length L_0 [m]. However, it is likely that the kinetic energy does not scale linearly with the length of the source, causing the decrease of e^*_{asymp} [−] with increasing Π_2 [−] (for $\Pi_2 > 30$) [−]. Therefore, the results in section 4.1.3 are all made with the same domain size $L_0 = 65$ m.

The condition set for Π_2 [−] in section 3.1.3.3 and 4.1.3 is:

$$\Pi_2 = \frac{L_0}{w} = 130 \tag{A.2}$$

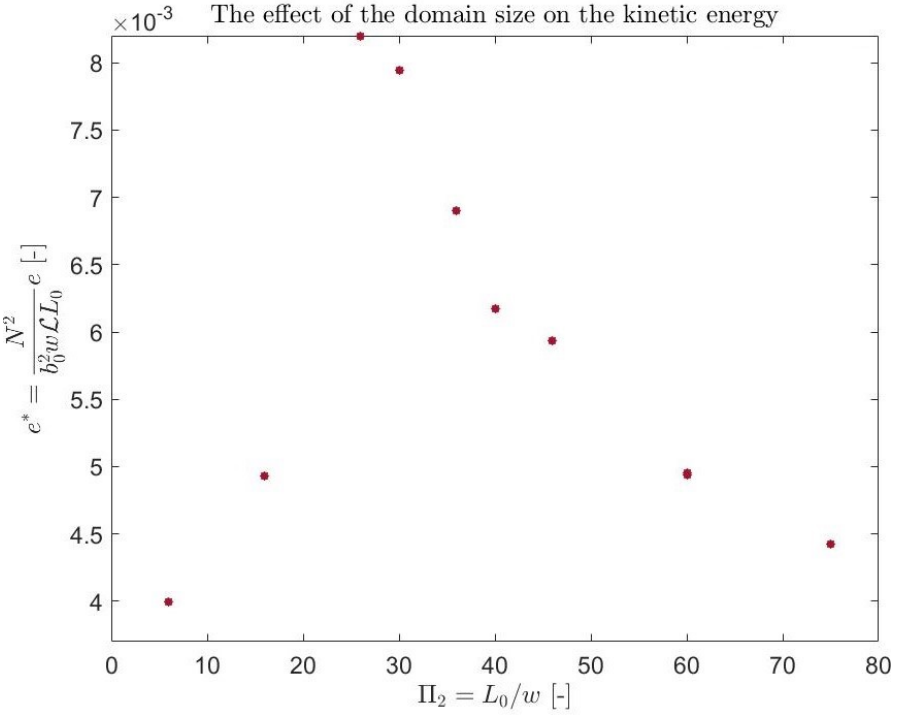

FIGURE A.6: The effect of the domain size L_0 [m], expressed as $\Pi_2 = L_0/w$ [−], on the asymptotic kinetic energy e^*_{asymp}.

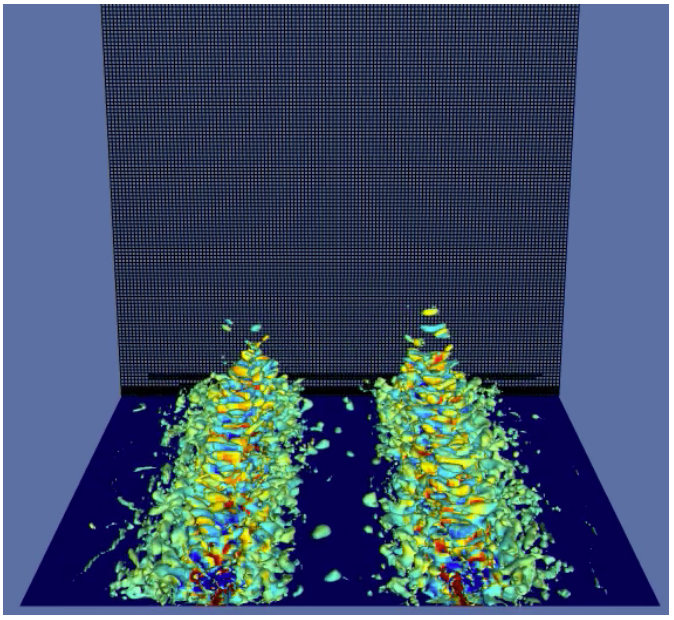

FIGURE A.7: The λ_2-isosurface [32] to show the vortices above the buoyancy heat sources. It can be seen that the 'walls' suppresses the voritices on the side, squeezing them and driving them upward.

A.4 Multiple heat sources (3D simulation): Effect of the viscosity

As an addition to the results of section 4.1.3, the effect of the viscosity on the kinetic energy is investigated with the setup of section 3.1.3.3. The viscosity is variable in the atmosphere, therefore its effect is interesting. A typical atmospheric condition is $\nu \approx 1.5 \cdot 10^{-5}\,\mathrm{m^2 s^{-1}}$ [25]. The effect of varying the viscosity is tested by adjusting the Reynolds number $\Pi_4 = b_0^2/N^3\nu\,[-]$. The values of the Reynolds number correspond to the viscosity range $\nu = (3.125 - 12.5) \cdot 10^{-5}\,\mathrm{m^2 s^{-1}}$. Figure A.8 shows that increasing the Reynolds number (i.e. decreasing the viscosity) decreases the kinetic energy in the system. At first sight, this is very counter-intuitive. But this relation is also influenced by the diffusivity $\kappa\,[\mathrm{m^2 s^{-1}}]$. Since the definition of the Prandtl number $\Pi_3 = \nu/\kappa = 1\,[-]$ causes the diffusivity $\kappa\,[\mathrm{m^2 s^{-1}}]$ to scale linearly with the viscosity $\nu\,[\mathrm{m^2 s^{-1}}]$. In a comparable study [12] the same effect is observed and it is shown that increasing the diffusivity and the viscosity (keeping the Prandtl number the same) yields an increased surface flux and thus more buoyancy enters the atmosphere. It can be seen in figure A.9 that indeed the surface flux increases with increasing viscosity and diffusivity (i.e. decreasing $\Pi_4\,[-]$).

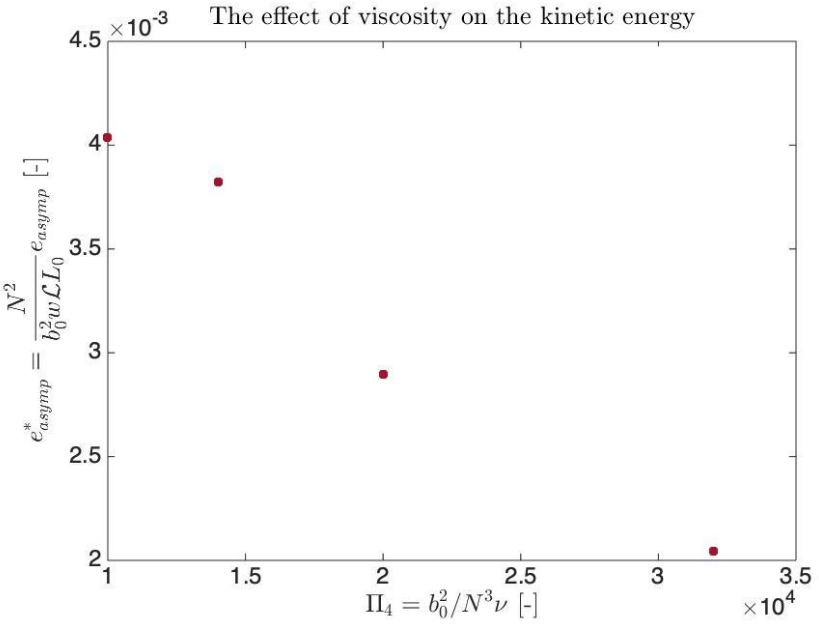

FIGURE A.8: The relation between the Reynolds number $\Pi_4\,[-]$ (changing the viscosity) and the kinetic energy for two sources a distance $d = 4\,\mathrm{m}$ apart in a domain $L_0 = 64\,\mathrm{m}$.

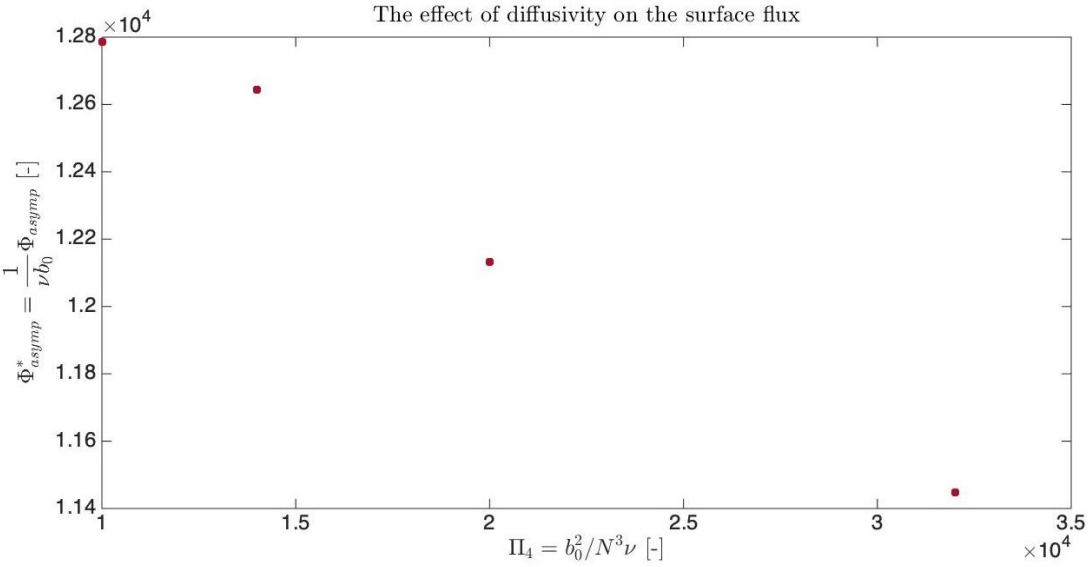

FIGURE A.9: The relation between the Reynolds number $\Pi_4\,[-]$ (changing the viscosity and diffusivity) and the surface flux for two sources a distance $d = 4\,\text{m}$ apart in a domain $L_0 = 64\,\text{m}$.

A.5 Multiple heat sources (3D simulation): Effect of the distance between the sources on the dissipation

In section 4.1.3 the effect of the distance between two sources on the kinetic energy is checked with the setup of section 3.1.3.3. At smaller distances ($\Pi_5 < 24\,[-]$), the kinetic energy decreases with increasing distances between the sources. At larger distances ($\Pi_4 > 24\,[-]$) this effect levels off. This same effect is observed on the asymptotic kinetic energy dissipation $-\epsilon^*_{asymp}\,[-]$, as can be seen in figure A.10. This makes sense since all the kinetic energy will eventually dissipate in a system that is in equilibrium.

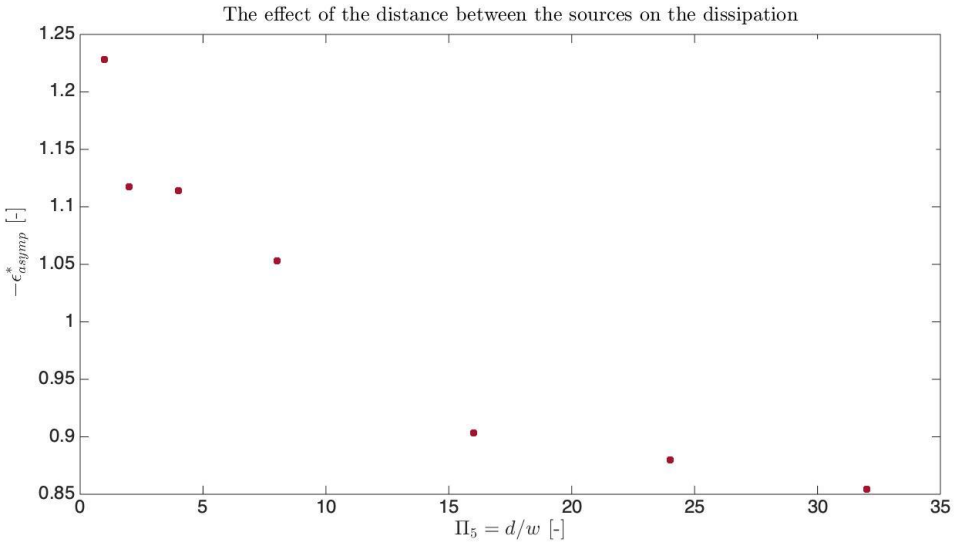

FIGURE A.10: The effect of the distance between two sources expressed in $\Pi_5 = d/w\,[-]$ on the total asymptotic dissipation $-\epsilon^*_{asymp}\,[-]$ in the system.

Appendix B

Experiment: Additional results

B.1 Unfiltered air temperature measured with the screen

The unfiltered results of the figures shown in section 4.2 are presented in this section.

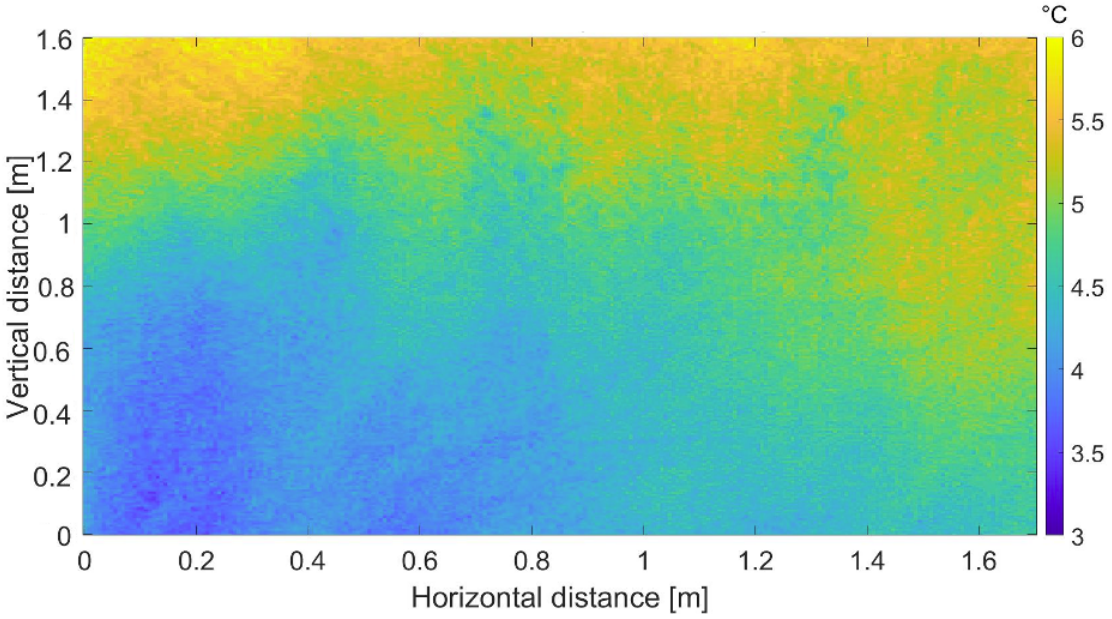

FIGURE B.1: A snapshot of the air temperature at 23:41:30 on April 13th in Krabbendijke without an averaging filter applied. This is the raw result of the result shown in figure 4.15.

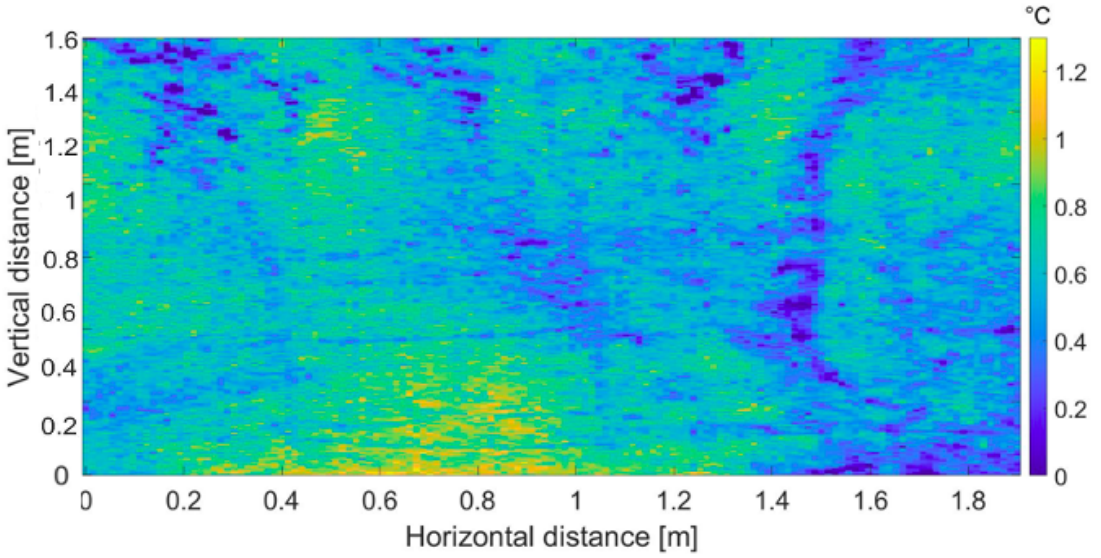

FIGURE B.2: A snapshot of the air temperature with two artificial heat sources (horizontal distance: $0.4 - 0.6\,\text{m}, 0.85 - 1.1\,\text{m}$) under the screen at 00:51:04 on April 14th in Krabbendijk without an averaging filter applied. This is the raw result of the result shown in figure 4.19.

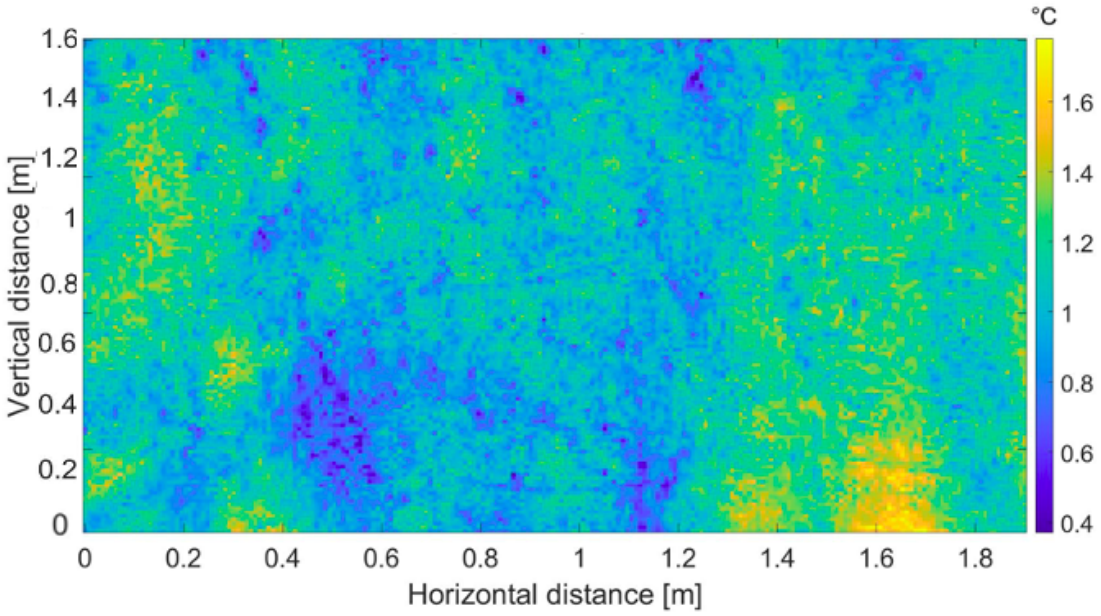

FIGURE B.3: A snapshot of the air temperature with two artificial heat sources (horizontal distance: $0.3 - 0.5\,\text{m}, 1.5 - 1.75\,\text{m}$) under the screen at 00:57:44 on April 14th in Krabbendijke without an averaging filter applied. This is the raw result of the result shown in figure 4.20.

B.2 Source temperature

The average temperature of the sources during all the measurements of section 4.2.2 are shown in figure B.4.

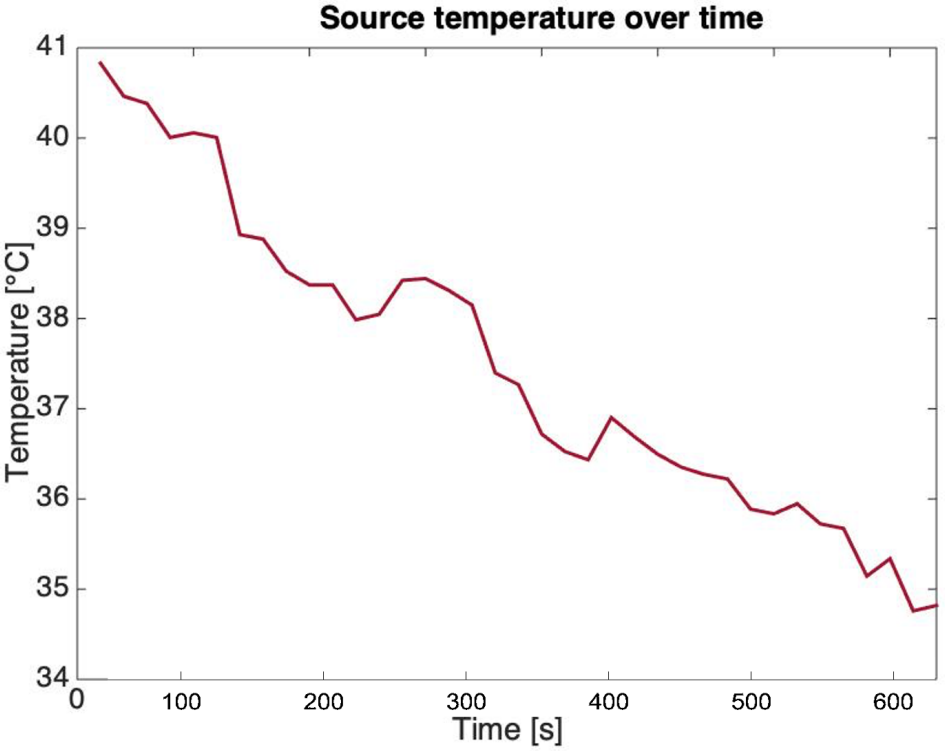

FIGURE B.4: The average temperature of the sources during the measurements of section 4.2.2.

Bibliography

[1] A.F. Moene and J.C. Van Dam. *Transport in the Atmosphere-Vegetation-Soil Continuum*. Cambridge University Press, 2014.

[2] M. Tjernström, M. Žagar, G. Svensson, S. Pfeifer J.J. Cassano, A. Rinke, K. Wyser, K. Dethloff, C. Jones, T. Semmler, and M. Shaw. Modelling the arctic boundary layer: An evaluation of six arcmip regional-scale models using data from the sheba project. *Boundary-Layer Meteorology*, 117:337–381, 2004.

[3] A.A. Baklanov, B. Grisogono, R. Bornstein, S.S. Zilitinkevich L. Mahrt, P. Taylor, S.E. Larsen, M.W. Rotach, and H.J.S. Fernando. The nature, theory, and modeling of atmospheric planetary boundary layers. *American Meteorological Society*, 2011.

[4] G. Svensson, A.A.M. Holtslag, V. Kumar, T. Mauritsen, G.J. Steeneveld, W.M. Angevine, E. Bazile, A. Beljaars, E.I.F. de Bruijn, and A. Cheng. Evaluation of the diurnal cycle in the atmospheric boundary layer over land as represented by a variety of single-column models: The second gabls experiment. *Boundary Layer Meteorology*, 140:177–206, 2011.

[5] A.A.M. Holtslag, G. Svensson, S. Basu, B. Beare, A.C.M. Beljaars, F.C. Bosveld, J. Cuxart, J. Lindvall, G.J. Steeneveld, M Tjernstroem, and B.J.H. van de Wiel. Stable atmospheric boundary layers and diurnal cycles: Challenges for weather and climate models. *Bulletin of the American Meteorological Society*, 94 (11):1691–1706, 2012.

[6] I. Sandu, A. Beljaars, and G. Balsamo. Improving the representation of stable boundary layers. *ECMWF*, 139:24–29, 2013.

[7] R. Stoll and F. Porte-Agel. Surface heterogeneity effects on regional-scale fluxes in stable boundary layers: Surface temperature transitions. *Journal Atmospheric Science*, 66:412–431, 2008.

[8] L. Mahrt. Variability and maintenance of turbulence in the very stable boundary layer. *Boundary-Layer Meteorology*, 135:1–18, 2010.

[9] I. Sandu, A. Beljaars, P. Bechtold, T. Mauritsen, and G. Balsamo. Why is it so difficult to represent stably stratified conditions in numerical weather prediction (nwp) models? *Journal of Advances in Modeling Earth Systems*, 5:117–133, 2013.

[10] X.M. Hu. Boundary layer (atmospheric) and air pollution | air pollution meteorology. In *Encyclopedia of Atmospheric Sciences (Second Edition)*, pages 227–236. Academic Press, Oxford, second edition edition, 2015.

[11] C. Akan. Surface mass transfer in large eddy simulation (les) of langmuir turbulence (doctoral dissertation). ***https://www.researchgate.net/publication/254706435_Surface_Mass_Transfer_in_Large_Eddy_Simulation_LES_of_Langmuir_Turbulence***, 2012.

[12] C.C. van Heerwaarden and J.P. Mellado. Growth and decay of a convective boundary layer over a surface with a constant temperature. *Journal of Atmospheric Science*, 73(50:2165–2177, 2016.

[13] S. De Roode. Atmospheric physics. ***http://www.srderoode.nl/Teaching/atmos_phys.pdf***, (accessed: 04-11-2020).

[14] A. Solcerova, F. van de Ven, and N. van de Giesen. Nighttime cooling of an urban pond. *Frontiers in Earth Science*, 7:156:1–10, 2019.

[15] J. Sun. Vertical variations of mixing lengths under neutral and stable conditions during cases-99. *Journal of Applied Meteorology and Climatology*, 50:10:2030–2041, 2011.

[16] E. Buckingham. The principle of similitude. *Nature*, 96:396, 1915.

[17] F.T.M. Nieuwstadt, B.J. Boersma, and J. Westerweel. *Turbulence: Introduction to theory and applications of turbulent flows.* Springer Nature, 2016.

[18] P. de Vrese, J.P. Schulz, and S. Hageman. On the representation of heterogeneity in land-surface-atmosphere coupling. *Boundary-Layer Meteorology*, 160:157–183, 2006.

[19] G.J. Steeneveld. Stable boundary layer issues. *ECMWF GABLS Workshop on Diurnal cycles and the stable boundary layer*, pages 25–36, 2011.

[20] S. Popinet. Basilisk. ***http://basilisk.fr***, (accessed: 03-11-2020).

[21] S. Popinet. An accurate adaptive solver for surface-tension-driven interfacial flows. *Journal of Computational Physics*, 228:5838–5866, 2009.

[22] S. Popinet et al. Gerris: a tree-based adaptive solver for the incompressible euler equations in complex geometries. *Journal of Computational Physics*, 190(2):572–600, 2003.

[23] L. Staron, P.Y. Lagrée, and S.Popinet. The granular column collapse as a continuum: validity of a navier-stokes model with a mu(i)-rheology. *Journal of Fluid Mechanics*, 686:78–4080, 2011.

[24] J.A. van Hooft, S. Popinet, and C.C. van Heerwaarden et al. Towards adaptive grids for atmospheric boundary-layer simulations. *Boundary-Layer Meteorology*, 167:421–443, 2018.

[25] J.A. van Hooft. *Modeling the Atmospheric Diurnal Cycle (Doctoral dissertation)*. Retrieved from Repositories TU Delft, 2020.

[26] B.J.H. van de Wiel, E. Vignon, P. Baas, I.G.S. van Hooijdonk, S.J.A. van der Linden, J.A. van Hooft, F.C. Bosveld, S.R. de Roode, A.F. Moene, and C. Genthon. Regime transitions in near-surface temperature inversions: A conceptual model. *Journal of the atmospheric sciences*, 74:1057–1073, 2017.

[27] A.M. Grudzielanek and J. Cermak. Capturing cold-air flow using thermal imaging. *Boundary-Layer Meteorology*, 157:321–332, 2015.

[28] A.M. Grudzielanek and J. Cermak. Temporal patterns and vertical temperature gradients in micro-scale drainage flow observed using thermal imaging. *Atmosphere*, 9(12):498, 2018.

[29] Optris. Infrared camera optris pi 400i / pi 450i. ***https://www.optris.global/thermal-imager-optris-pi-400i-pi-450i***, (accessed: 28-4-2021).

[30] Fruvo B.V. Fruitcultures. ***https://www.fruvo.nl/***, (accessed: 1-6-2021).

[31] LabIR. Thermographic paint for standard applications. ***https://labir.eu/?_ga=2.224934810.1054246799.1620909235-2119225429.1620909235***, (accessed: 13-5-2021).

[32] J. Jeong and F. Hussain. On the identification of a vortex. *Journal of Fluid Mechanics*, 285:69–94, 1995.

[33] V.W.J. Heusinkveld, J.A. van Hooft, B. Schilperoort, P. Baas, M. ten Veldhuis, and B.J.H.van de Wiel. Towards a physics-based understanding of fruit frost protection using wind machines. *Agricultural and Forest Meteorology*, 282-283:107868, 2020.